UNIVERSITY OF CRETE
DEPARTMENT OF PHYSICS

Degree Thesis

X-ray variability studies with Swift/BAT light curves

Manoura Ilektra

Supervisor:
Prof. Papadakis Iossif

Heraklion, March 2022

ACKNOWLEDGMENTS

CONTENTS

CHAPTER 1. INTRODUCTION

1.1) Observations of Active Galactic Nuclei

In 1908, E. A. Fath at Lick Observatory was the first person to take the optical spectrum of an active galaxy and he noted the presence of strong emission lines in NGC1068. Later, V. M. Slipher, at Lowell Observatory, obtained a higher resolution spectrum and noted that the emission lines are very similar to those observed in planetary nebulae. Active galaxies were first recognized as a separate class of objects by Seyfert, in 1943. Seyfert found that some galaxies contain bright nuclei, emission lines from highly ionized atoms, and that some hydrogen emission lines are significantly broadened. The galaxies showing such features are currently called "Seyfert galaxies".

Seyferts were first classified as Type 1 and Type 2, depending on the emission lines shown by their spectra. In some cases they are classified as an intermediate type. Type 1 Seyfert galaxies are very bright sources of ultraviolet light and X-rays with optical spectra that shows broad lines, with widths up to 10^4 km s^{-1}, that include both permitted lines, like H I, He I or He II and narrower forbidden lines, like O III.

Class	Sub-Class	Features
Seyfert	Type 1	narrow and broad emission lines, X-ray emission, weak radio emission, spiral galaxies
	Type 2	narrow emission lines, weak radio and X-ray emission, spiral galaxies, less variable
Quasars	Radio-loud (QSR)	narrow and broad emission lines, strong radio emission, polarization, FR II
	Radio-quiet (QSO)	narrow and broad emission lines, weak radio emission and weak polarization
Radio Galaxies	BLRG	narrow and broad emission lines, strong radio emission, weak polarization, elliptical galaxies, FR II
	NLRG	narrow emission lines, strong radio emission, FR I and II, elliptical galaxies, not variable
Blazars	BL Lacs	lack of emission lines, strong radio emission and strong polarization, elliptical galaxies, rapidly variable
	OVV Quasars	much more luminous BL Lacs with both narrow and board emission lines
LINERs		similar to Seyfert 2 with low luminosity, low ionization emission lines, alternatively: stardust phenomena or HII emission region

Table 1.1 *A Summary of AGN Classes and Sub-classes ,with their basic features.*

The spectra of Type 2 Seyfert galaxies show only permitted and forbidden narrow lines, produced by a low density ionized gas with widths from 200 to 900 km s^{-1}. Forbidden lines are spectral lines that occur due to electron transitions not normally allowed by the selection rules of quantum mechanics, but that still have a small probability of spontaneously occurring. The sub-classes Type 1.2, 1.5, 1.8 and 1.9 have weaker broad lines relative to the narrow lines as the number of type increases. The difference among types is probably due to our different point of view.

Seyfert galaxies belong to the general class of galaxies which are called Active Galactic Nuclei, AGN for short. Active galaxies account for about 10% of all galaxies in the nearby universe. There are other AGN classes, as shown in Table 1.1. There are several common phenomena that are observed in all AGN, such as:

- Bright star-like compact nucleus with bolometric luminosity from 10^{43} to 10^{49} erg s^{-1}, powered from region that with dimension not much larger than our Solar System.

- A wide continuum and non-thermal spectrum, as shown at Fig.1.1, with the energy flux given by the power law of the form

$$F_\nu \propto \nu^\alpha \quad ,$$

  where ν is the frequency.
- Variability in all wavelengths, with timescales that range from hours/days to years. The variability amplitude increases with increasing frequency.
- Strong emission lines in the optical band, usually from hydrogen and sometimes from heavier elements such as helium, oxygen, iron ect, which can be broadened due to Doppler effect (Fig.1.2).

Although there are also some difference, such as the presence or the absence of broad emission lines, the strength of radio and X-ray emission, and the existence or not of jets, all AGN are probably powered by the same engine.
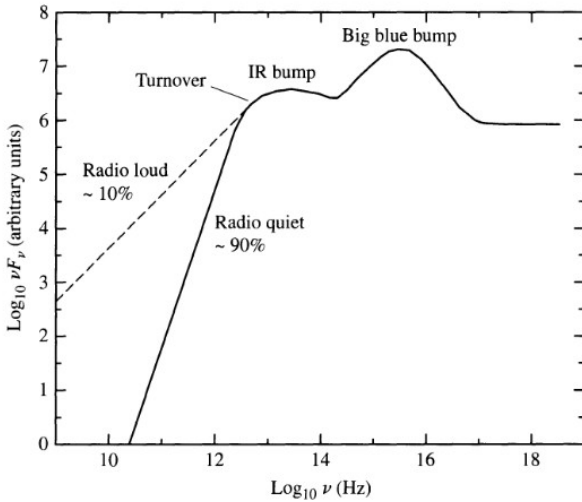

Figure 1.1 *The continuum observed from many AGNs. (Taken from Caroll & Ostlie "An Introduction to Modern Astrophysics")*
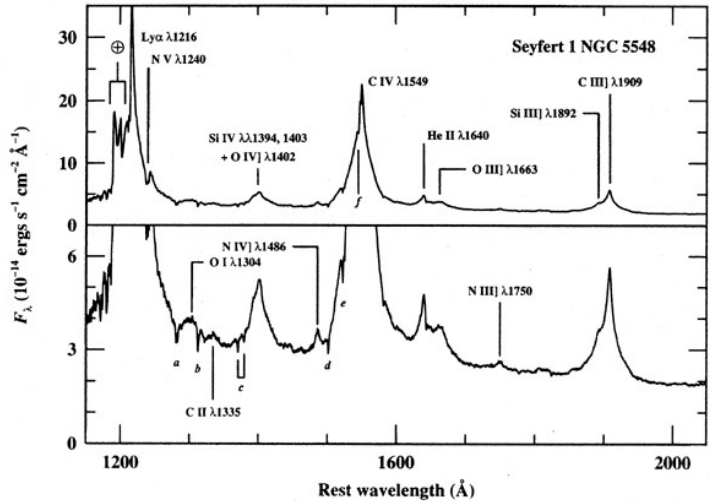
Figure 1.2 *The ultraviolet spectrum of the Seyfert 1 galaxy NGC 5548. The prominent broad emission lines are labeled. (Taken from Peterson "An Introduction to Active Galactic Nuclei")*

1.2) The Nature of the Central Engine of AGN

The size of an emitting source can be estimated from the timescale of a significant variation of the emitted luminosity. For example, let us consider a source, with a radius of *r*, which varies in flux by a factor of 2, or more. In this case, due to causality reasons the size of the emission region, should obey the following relation:

$$r \leq c \cdot \Delta t \quad .$$

The fastest variations are observed in the X-ray band, Δt can be less than a few hours. This implies that the radius of the X-ray source should be less than a few AU. At the same time, as I mentioned above, luminous AGN have bolometric luminosity from 10^{43} to 10^{49} erg s^{-1}, while the X-ray luminosity is larger than 10^{42} erg s^{-1}. Therefore, in AGN, we need a source of radiation which must be very efficient, in order to produce large amount of power in a small region.

Today we believe that the main source of power in AGN is the accretion of matter to a supermassive black hole at the center of the host galaxy. This process can explain the large luminosity emitted from a small region. In general we expect the in-falling material to form an accretion disc around the black hole, converting gravitational energy into thermal energy and radiation. Here is an example of how efficient this process can be.

Let us assume a particle, with mass m, falling from r_∞, to a distance r_{in} from a central mass, M_{BH}. The change in potential energy in this case is:

$$\Delta E = \frac{-GM_{BH}m}{r_{in}} \quad .$$

For a nonrotating black hole, the smallest stable circular orbit for a particle is at $r = 3R_S$ where R_s is the Schwarzshild radius. This radius determines the size of the system, and is defined as:

$$R_S = 2\frac{GM_{BH}}{c^2} \quad .$$

Therefore, if $r_m = 3R_S$, the released energy will be:

$$\Delta E = \frac{GM_{BH}}{3R_s}m \quad .$$

According to the Virial theorem, half of the potential energy will convert to kinetic energy and the other half will be available to heat the material and radiate. Therefore, the available energy for radiation will be:

$$E_{rad} = \frac{\Delta E}{2} = \frac{1}{2}\frac{GM_{BH}}{3R_s}m = \frac{1}{12}mc^2 = \eta mc^2 \quad ,$$

where η is the efficiency of the matter accretion to the central BH. The equation above shows that it can reach a value of ~0.1, which is much larger than the efficiency of thermonuclear reactions (ε~0.008).

1.3) X-ray emission of AGN

AGN are very luminous in X-rays. If the X-ray emission is due to thermal emission from the disk, the disk temperature should be $T \sim 10^7 - 10^9 K$. However, the accretion disk in AGN cannot be that hot. It is generally believed that X-rays in AGN are emitted by inverse Compton scattering of the optical and UV photons that are emitted from the disk by hot electrons, with temperature of $\sim 100\,keV$. The hot electrons are probably located at a small region, above the central BH, which is usually called as the "X-ray corona".

The X-ray emission is quite variable, and can change appreciably on timescales ranging from hours to days/ months. As an example I present, in Fig. (1.3), the monthly lightcurve of a Seyfert 1 galaxy, namely NGC 4151, observed by the BAT instrument on board NASA'a *Swift* satellite. Figure (1.3) shows that the source is variable at all sampled time-scales, from 2 months to years. Actually, the flux can double within a month (see variation from month 32 to month 33). The lowest and the highest source count rate is shown with two vertical red dashed lines. Their ratio indicates a variation by a factor ~5.5, over a time period of 4.17 years.

The main object of this project is to study the variability amplitude of the X-ray emission in AGN, using lightcurves from the BAT instrument. This instrument detects photons in the energy range of 15-150 keV. A hard X-ray, all-sky survey, with an energy range above 10 keV gives the opportunity to study astrophysical objects, because energetic hard X-ray photons can pass through large columns of gas and dust at these energies. That cannot be achieved in lower energy X-rays because they are easily absorbed. Therefore the *Swift*-BAT all-sky hard X-ray survey is very important in the study of the X-ray variability of both Seyfert I and II galaxies.
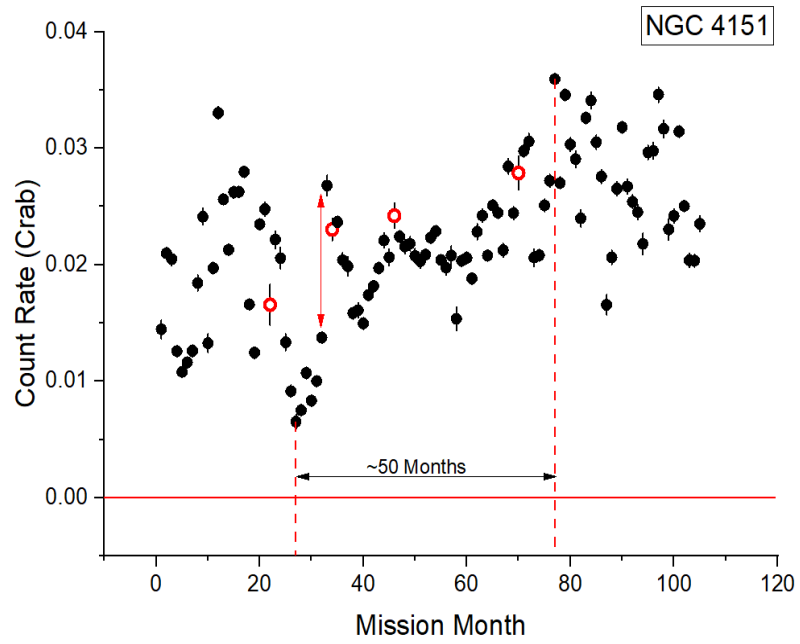
Figure 1.3 *The 14-195 keV lightcurve of NGC 4151. The count rate is measured in Crab units. The red line shows zero count rate.*

CHAPTER 2. THE *SWIFT* BAT SURVEY

2.1) The Neil Gehrels Swift satellite

All the data used for this project were collected by the NASA's Neil Gehrels *Swift* Observatory, which was launched on 20 November 2004. The main objective of the satellite was to detect gamma-ray bursts (GRBs), and the monitor of their afterglows in the gamma-ray, X-ray, ultraviolet, and optical wavebands. *Swift* rotates at a radius of approximately 550 km above the surface of Earth, (i.e. it has a low Earth orbit) and completes a full rotation every 95.74 minutes.
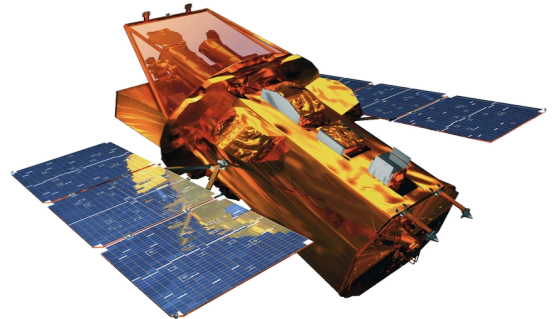
Swift carries three telescopes on board: **1)** the X-ray Telescope (XRT) **2)** the Ultraviolet/Optical Telescope (UVOT) and **3)** the Burst Alert Telescope (BAT). The XRT is a sensitive X-ray CCD imaging spectrometer at the focal plane of an X-ray

Figure 2.1 *NASA's Swift Gamma Ray Burst Detecting satellite*

telescope with a 3.5 m focal length. It covers the energy range of 0.2-10 keV. The XRT can take images and perform spectral analysis. The UVOT is an optical and ultraviolet (UV) 30 cm aperture telescope. It has 6 broad-band filters operating over the range of 170-650 nm, plus two grisms, one optical and one UV. The UVOT is used to detect the optical afterglow of GRBs, and is used to provide long-term follow-ups of GRB afterglow lightcurves. The XRT and UVOT are co-aligned and are pointed near the center of the BAT Field-Of-View (FOV). The BAT detects GRB events and computes its coordinates in the sky. It can detect photons in the energy range of 15-150 keV.

2.2) The Swift BAT survey

The Burst Alert Telescope is a highly sensitive, wide FOV ($\sim 60° \times 100°$) instrument. The prime objective of the instrument is the fast detection of a gamma-ray burst. It is a coded aperture imaging instrument with a 1.4 steradian field-of-view (it can monitor simultaneously 11% of the sky). The BAT uses a two-dimensional coded aperture mask and a large area solid state detector array to detect weak bursts, and has a large FOV to detect a good fraction of bright bursts.

The BAT runs in two modes: **1)** burst mode, which produces burst positions, and **2)** scan-survey mode. Most of BAT's time is spent waiting for a burst to occur. While searching for bursts, BAT performs an all-sky hard X-ray survey and monitors hard X-ray transients. The *Swift*-BAT detects sources of primarily extragalactic nature, mainly AGN and some clusters. The BAT accumulates detector plane maps every five minutes, which are included in the normal spacecraft telemetry stream.

Three catalogs of sources detected during the hard X-ray survey have been published so far. Tueller et al. (2010) provided a catalog based on the analysis of the first 22 months data. Baumgartner et al. (2013) published eight-channel spectra as well as monthly lightcurves from the first 70 months of data with improved data processing. The latest one is the 105-month *Swift*-BAT all-sky hard X-ray survey published by Oh et al. (2018). For this project I used the lightcurves from the latest 105-month *Swift*-BAT survey (hereafter *105-SBs*), thus I provide further information about this survey in the section below.

2.3) The 105-month Swift-BAT all-sky hard X-ray survey

Oh et al. (2018) published the results from the BAT hard X-ray all-sky survey using the data from the first 105 months of operation, including observations carried out between 2004 December and 2013 August.

Until then, *Swift*-BAT had observed over 50% of the sky with more than 15.3 Ms of exposure time, while the 40% of the sky was covered with 11.4 Ms. As a result the *105-SBs* reaches a sensitivity of 7.24×10^{-12} erg s^{-1}
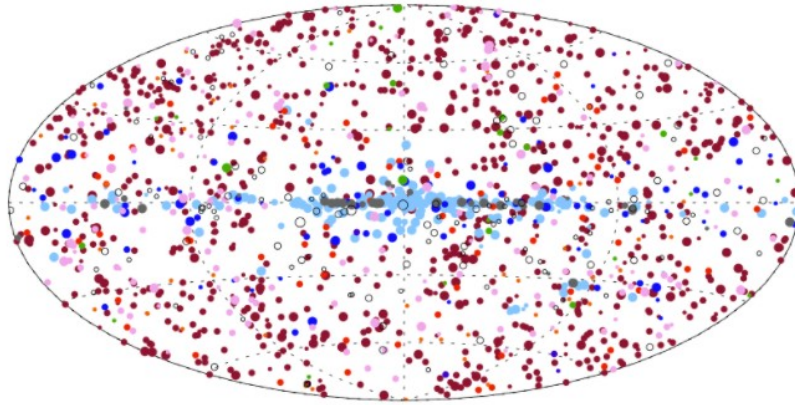
cm^{-2} over 50% of the sky in the 14−195keV band, and 8.40×10^{-12} erg s^{-1} cm^{-2} over 40% of the remaining part.

The *Swift*-BAT 105 month catalog (hereafter *105-SBc*) lists 1632 hard X-ray sources in the 14−195 keV band, which have been detected above the 4.8σ significance level. Table (2.1) lists the number of sources per each source type. AGN of all types (i.e. class 40-80) account for 67% of all sources. In fact, 34% of the new detections in the *105-SBs* (144 of the 422 new detections) are identified as Seyfert AGN in nearby galaxies ($z < 0.2$). Seyfert I and II are the most popular source types in the *105-SBs*. There are 827 Seyfert I and Seyfert II galaxies out of the total 1632 sources in the *105-SBc*. In other words more than 50% of all sources in the *105-SBc* are Seyfert AGN.

2.4) Seyferts in the BAT survey

As mentioned above *Swift*-BAT detects a large number of AGN, primarily Seyfert I and II AGN. In fact 827 sources out of 1099 AGN are identified as Seyfert galaxies. There are two subcategories: "Seyfert I", which includes Sy 1.0 to 1.8 types and "Seyfert II", that includes the remaining Sy 1.9 to 2.0 types. According to the AGN unification theory, the observational differences between Seyfert I and Seyfert II are due to differences in the inclination angle. However, I would like to test whether the two types of Seyferts have the same variability properties, so in the "SyI" sample I kept only the Seyfert types from 1 up to 1.5, while the "SyII" sample includes all the types from 1.9 to 2.

Figure (2.3) shows the histogram of the 14−195 keV flux (F_{14-195}, hereafter) and redshift, z, of the Seyfert galaxies in the *105-SBc* (panel **a** and **b** respectively). Black filled bars show the distribution of the SyI data and red open bars show the distribution of the SyII data. All the data are drawn from Table (A.1) in the

Class	Source Type	# in Catalog
10	Unknown class I	36
11	Unknown class II	55
12	Unknown class III	38
15	Multiple	10
20	Galactic Center	1
30	Galaxy Cluster	26
40	Seyfert I (Sy 1.0-1.8)	379
50	Seyfert II (Sy 1.9-2.0)	448
60	LINER	6
70	Unknown AGN	114
80	Beamed AGN (Blazar/FSRQ)	158
90	Cataclysmic Variable Star (CV)	75
100	Symbiotic Star	4
110	Other Star	12
120	Open Star Cluster	1
130	Starburst Galaxy	1
140	Compact Group of Galaxies	1
150	Pulsar	25
160	Supernova Remnant (SNR)	7
170	Nova	6
180	High Mass X-ray Binary (HMXB)	108
190	Low Mass X-ray Binary (LMXB)	109
200	Other X-ray Binary (XRB)	8
210	Globular Cluster (GC)	1
220	Molecular Cloud	2
230	Gamma-ray Source	1
	Total	1632

Table 2.1: Catalog of all the source types in the Swift-BAT all-sky X-ray survey and the number of objects detected in each one. The box indicates the various AGN types in the survey.

Appendix. By looking at Fig. (2.3), the SyI and SyII distributions of F_{14-195} appear to be similar. In contrast, the z distributions seem to be different. It appears that the SyI galaxies have larger z. The SyI galaxies appear to be more distant, on average, than SyII galaxies.

I calculated the mean, the median and the standard deviation of the two distributions. Table (2.2) lists the modes of the F_{14-195} and z distribution of the SyI and SyII samples (first and second row). The second and sixth columns list the mean and median (values in parenthesis) of the F_{14-195} and z distributions, respectively. Third and seventh columns list the standard deviation, σ, of the distributions.

Type	$\overline{F}_{14-195}$ $(10^{-12}\ erg\ s^{-1}\ cm^{-2})$	σ_F $(10^{-12}\ erg\ s^{-1}\ cm^{-2})$	D_F	$p_{null,F}$	$\overline{z}$	σ_Z	D_z	$p_{null,z}$
Sy I	24.30 (13.81)	41.38	0.08	0.11	0.092 (0.056)	0.206	0.29	2.54 10^{-14}
Sy II	24.34 (15.00)	35.4			0.042 (0.03)	0.047		

Table 2.2: *Columns 2,3 and 6,7 list the mean, median and standard deviation of the distribution of F_{14-195} and z of the SyI and SyII galaxies. Columns 4,5 and 8,9 list the Kolmogorov–Smirnov statistic D and the probability p_{null}, from the comparison of the two distributions.*

From these results it appears that the F_{14-195} distributions are similar. The values of mean are almost the same and the values of median are close. However, the values of standard deviation are different. The $\sigma_{F,SyI}$ appears to be larger than $\sigma_{F,SyII}$. This happens because there are quite a few SyI galaxies with fluxes larger than the mean flux. In general, the results about the F_{14-195} ,listed in Table (2.2), agree with the shape of the distribution shown in Fig. (2.3)(left panel).

The results presented in Table (2.2) indicate that the z distributions are different. The mean of z_{SyI} is larger than z_{SyII}. This happens because there are three SyI galaxies with $z > 0.6$ (these points do not appear in the right panel of Fig. (2.3)). That also explains why σ_{zSyI} is that large. Without these points the results are: $\overline{z}'_{SyI} = 0.075(0.054)$ and $\sigma'_{SyI} = 0.067$. However, the mean and median of the two distributions are still quite different. The SyI mean and median redshifts are larger than the corresponding ones for SyII.

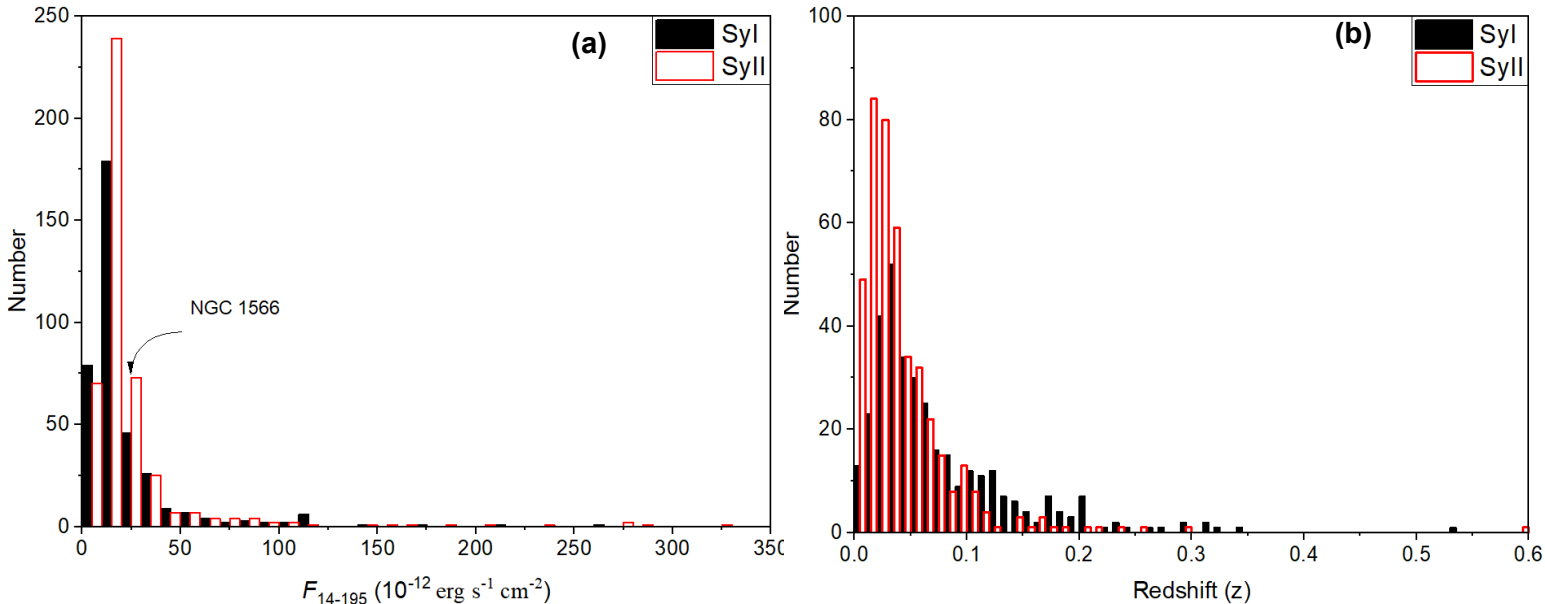
Figure 2.3: *Sample distribution of F_{14-195} and z (panel **a** and **b** respectively). Black filled bars correspond to SyI and red open bars to SyII sources.*

I performed the two sample Kolmogorov-Smirnov (K–S) test in order to investigate if F_{14-195} and z distributions are the same for the SyI and SyII samples. In statistics, the K–S test is a test of the equality of one-di-

mensional probability distributions that can be used either to compare a sample with a reference probability distribution (one-sample K–S test), or to compare two sample distributions (two-sample K–S test).The Kolmogorov–Smirnov statistic is defined as:

$$D = \max_{-\infty < x < \infty} \left| S_{N1}(x) - S_{N2}(x) \right| \quad , \qquad (1)$$

where S_{N1} and S_{N2} are the cumulative distribution functions of the two samples and D quantifies the maximum distance between them. The distribution of this statistic is computed under the null hypothesis that the samples are drawn from the same distribution. The null hypothesis can be rejected if the probability, p_{null}, that D would have the derived value by chance, is below 1%.

I used the Python command *"ks_2samp"* from the library *"scipy.stats"* to derive the statistic and the p_{null} of the K-S test. The results for the distributions of F_{14-195} are: $D_F = 0.08$ and $p_{null,F} = 0.11$. Since $p_{null,F} = 11\% > 1\%$, I conclude that the F_{14-195} distributions of the SyI and SyII samples are consistent with being drawn from the same distribution. For the distributions of redshift the results are: $D_z = 0.29$ and $p_{null,z} = 2.54 \ 10^{-14}$, which indicates that the two distributions are different. I repeated the K-S test without the three points with $z > 0.6$ and the results did not change notably. The K-S test results, the difference on the sample mean and median, and the appearance of the two distributions in the right panel of Fig. (2.3) agree with the fact that the distance of the SyI sources is systematically larger than the distance of the SyII sources.

2.5) The BAT lightcurves

The *105-SBs* released monthly lightcurves for each source in the catalog. Most of the work for this project is based on analysis of these lightcurves. I downloaded the ligthcurves from the *Swift* BAT 105-Month Hard X-ray Survey: Source Catalog (https://swift.gsfc.nasa.gov/results/bs105mon/). The count rate (*CR*) is background subtracted, and normalized in *Crab* units. The Crab nebula has a particular importance in X-ray and gamma-ray studies, as it has been used as a standard candle. The Crab flux in the $14 - 195$ keV band is 2.3343×10^{-8} erg cm^{-2} s^{-1}, and it defines the *Crab* unit.

As an example of the quality of the BAT lightcurves, I plot the lightcurves of two galaxies, namely NGC 4151 and NGC 1566 in Fig. (2.4). NGC 4151 (number 595 in the catalog) hosts one of the brightest AGN known at X-ray wavelengths. It is the brightest among Seyfert galaxies in the BAT catalog, with $F_{14-195} = 618.88 \ 10^{-12}$ erg s^{-1} cm^{-2}. The second source, NGC 1566 (number 216 in the catalog) has a flux which is near to the median of the SyI distribution ($F_{14-195} = 19.54 \ 10^{-12}$ ergs s^{-1} cm^{-2}).
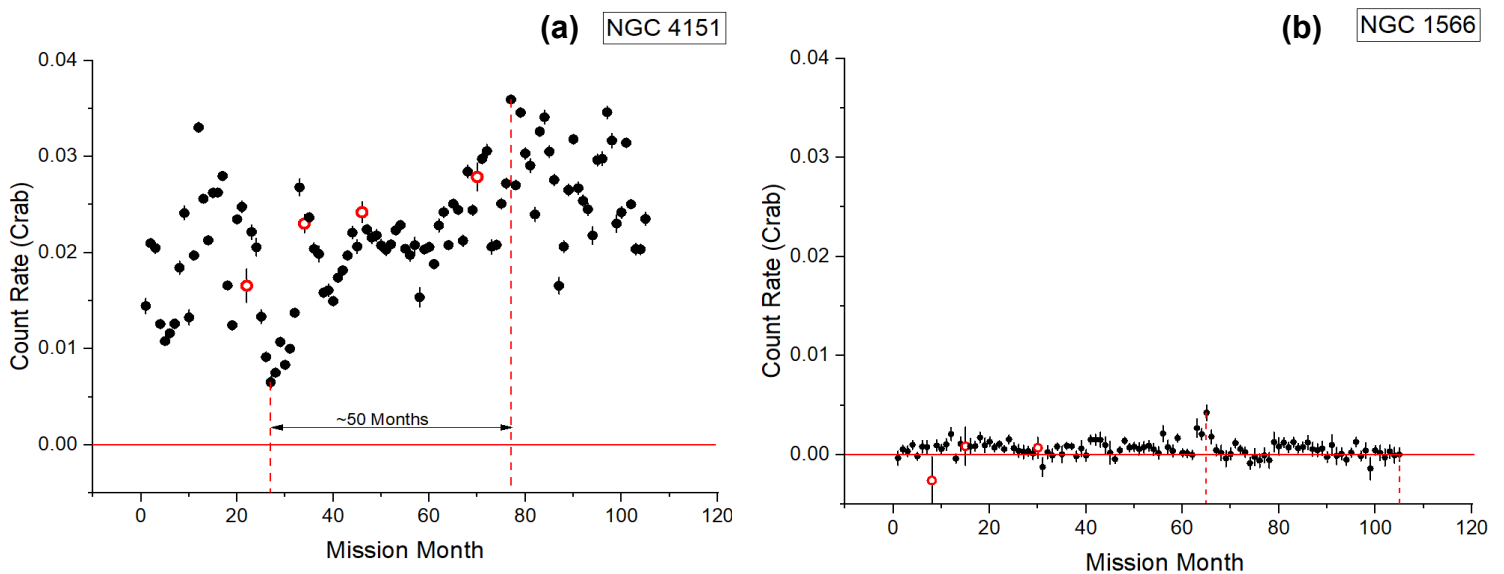

Figure 2.4 The 14-195 keV lightcurve of NGC 4151(a) and NGC 1566(b), count rate is measured in Crab units. The red line shows zero count rate. Red empty circles represent observations points with exposure time less than 40 ksec.

The two plots in Fig. (2.4) have the same limits in y-axis, so they can be compared. Left panel in Fig. (2.4) shows that NGC 4151 is extremely variable on all sampled time scales. For example, the two vertical red dashed lines, in Fig. (2.4**a**), show the lowest and the highest source count rate. Their ratio indicates a variation by a factor ~5.5, over a time period of 50 months. In addition there is a case that the rate doubles within a month (month 32 to 33). Figure (2.4**b**) shows the lightcurve of NGC1566. This source has low count rate. Red line in both plots shows the value of zero count rate, and most of the points in the lightcurve of NGC1566 are close to it. NGC1566 shows variations, despite its low count rate. The ratio indicates a variability factor by two orders of magnitude, mainly because the lowest count rate is close to zero. The lowest count rate is $3.4 \cdot 10^{-5}$ *Crab* and the highest $4.2 \cdot 10^{-3}$ *Crab,* at 65th and 105th mission month respectively, as show by the red dashed lines.

2.6) The errors of BAT lightcurves

The BAT 105-month lightcurves show the count rate of photons (photons/sec) that BAT detects every month. In reality, sources emit power (i.e. erg/sec). The total amount of energy crossing the detector per unit time divided by the area of the detector is the observed source flux $f(t)$ in units of $\mathrm{erg\ cm^{-2}\ s^{-1}}$. The flux is converted to a number of photons in a time period between t and $t + \Delta t$ as follows:

$$R \int_{t}^{t+\Delta t} f(t)dt \Rightarrow N_{ph,obs}(t) \ , \qquad (2)$$

where R is the so-called instrumental response. Roughly speaking R determines the number of photons that the detector will detect, when observing a source with flux $f(t)$. However, the *Swift*-BAT, like every detector, also detects background radiation, i.e. $N_{ph,obs}(t) = N_{ph,source}(t) + N_{ph,backg}(t)$. Therefore, the net source count rate will be:

$$CR_{source}(t) = \frac{N_{ph,obs}}{\Delta t} - \frac{N_{ph,backg}}{\Delta t} = CR_{obs}(t) - CR_{background}(t) \ , \qquad (3)$$

where Δt is the bin size of the lightcurve.

Even if a telescope is observing a source with a constant flux, the number of photons the detector will detect will be variable, due to the experimental noise. The number of photons detected by any detector follows a Poisson distribution, which means that the mean and the variance of the photon's distribution are equal. Based on this, the count rate error, $\sigma_{CR,source}^2$, will be given by the equation:

$$\sigma_{CR,source} = \sqrt{\frac{\sigma_{ph,obs}^2}{\Delta t^2} + \frac{\sigma_{ph,backg}^2}{\Delta t^2}} = \sqrt{\frac{N_{ph,obs}}{\Delta t^2} + \frac{N_{ph,backg}}{\Delta t^2}} = \frac{1}{\Delta t}\sqrt{\sigma_{ph,obs}^2 + \sigma_{ph,backg}^2} \ , \qquad (4)$$

where I have approximated the mean of the distribution with the observed count rate, and used the fact that $\sigma_{ph}^2 = N_{ph}$ for the Poisson distribution. Δt is the actual exposure time. Formally, Δt equals to one month in the BAT lightcurves (this is the bin size of the BAT lightcurves). However BAT does not observe a single source for 1 month continuously. Typically, BAT observes a source for some hours (up to ~3 days) every month. The time period it observed each source every month is the exposure time Δt.

Figure (2.5) shows plots of σ_{CR} as function of Δt for NGC 4151 and NGC 1566 (panel **a** and **b** respectively). Observing the two plots we can see that despite their different count rate, the errors of the points in the lightcurves are similar: they range from 0.0002 to 0.01 *Crab* for both sources. This can only happen when the error of a source, $\sigma_{CR,source}$ is dominated by the error of background noise, $\sigma_{CR,back}$. According to the equation (4) this happens when $N_{ph,backg}(t) \gg N_{ph,source}(t)$, in which case I expect the count rate error to be:

$$\sigma_{CR,source} \simeq \sqrt{\frac{CR_{backg}}{\Delta t}} \ , \qquad (5)$$

In other words I expect σ_{CR} to be inversely proportional to square-root of exposure time Δt. The red solid line shows the function $\sigma_{CR,source} = c/\sqrt{\Delta t}$, with, $c \simeq 0.23\,Crab^{1/2}$ that provides a good fit to the points in both plots.

The vertical red solid line plotted in both plots of Fig. (2.5) indicates the exposure time Δt =40 ksec. By taking out the points on the left of that line, i.e. the points with Δt<40ksec, the remaining errors of the points in the lightcurve are quite similar, they vary by a factror of ~3 (from ~0,0003 to 0,001). Since I will study the excess variance (more information about the excess variance at the next chapter), the determination of the mean experimental error is important. Large errors will dominate the mean value and as a result the internal variability amplitude may be underestimated. Therefore, I choose to ignore the points with Δt <40 ksec.
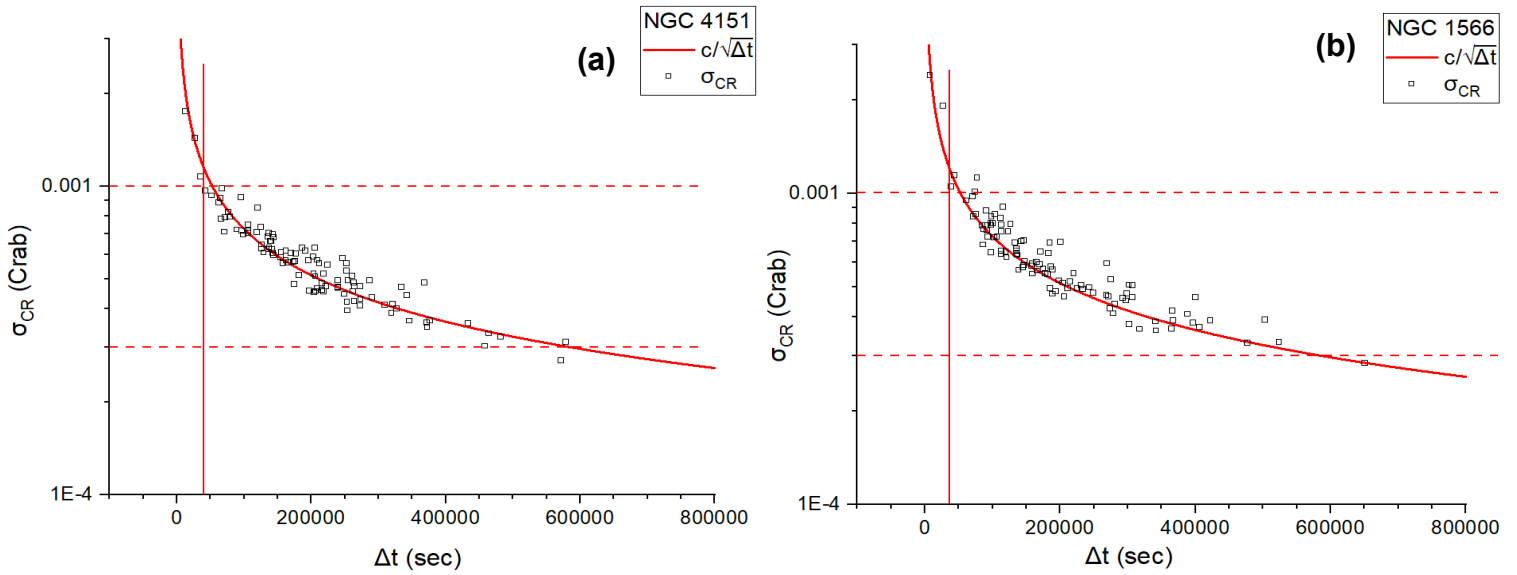
Figure 2.5 Plots of σ_{CR} as function of Δt for NGC 4151(a) and NGC 1566(b). Red solid line shows the function $y=0.23/\sqrt{\Delta t}$.

CHAPTER 3. THE EXCESS VARIANCE

The main objective of my work is to calculate the excess variance using the lightcurves from the *105-SBs*. The reason why I wish to compute this will be clear at the next chapter.

The variance of the lightcurve measures the scatter of the points around their mean. Variance is introducted both by the intrinsic variability of the source, and the experimental measuring process. For that reason, in order to measure the intrinsic variability amplitude of an AGN, we do not calculate the variance itself, but the so called "normalized excess variance" which is defined as follows (Nandra et al. 1997):

$$\sigma^2_{NXV} = \frac{1}{N\,\bar{CR}^2} \sum_{i=1}^{N} [(CR_i - \bar{CR})^2 - \sigma^2_{CR,i}] \quad , \qquad (6)$$

where N is the number of observations, CR_i is the count rate, $\sigma_{CR,i}$ is the experimental error of each observation in the i th bin, and $\bar{CR}$ is the mean count rate. For most of the sources in *105-SBs*, N goes up to 105, but there are 22 sources in the samples, with N <105. Most of these lightcurves only miss a month, there are 3 sources with N =104, and only one with N =103.

The excess variance, as defined by eq. (6), is a sum of two terms. The first term, $\sum_{i=1}^{N} (CR_i - \bar{CR})^2 / N$, is the variance of the lightcurve. The second term $\sum_{i=1}^{N} \sigma^2_{CR,i} / N$, is the mean square experimental error. As I already discussed in section (2.6), a part of the observed variations are caused by the experimental error. Even if the source has a constant intrinsic flux the observations will appear to be variable, due to the Poisson noise process. The statistic σ^2_{NXV} is called "excess" variance because the contribution of the experimental process is subtracted from the total variance of the lightcurve. In this it is representative of the intrinsic variability of the source.

It is also called "normalized" excess variance because the excess variance is divided with the mean square count rate $\bar{CR}^2$. This is done in order to derive a dimensionless variance which will indicate the average scatter of the points as a percentage of the mean count rate. In this way, σ^2_{NXV} calculated using the BAT lightcurves can be compared with σ^2_{NXV} computed with lightcurve from different telescopes for the same source. Even the values of σ^2_{NXV} for different sources can be compared. So the normalized excess variance helps to characterize the variability amplitude of astrophysical sources such as AGN.

3.1) The excess variance and the *S/N* ratio

The signal-to-noise (*S/N*) ratio of a lightcurve is defined as:

$$S/N = \frac{\bar{CR}}{\bar{\sigma}_{CR}} \quad , \qquad (7)$$

where $\bar{CR}$ is the mean count rate and $\bar{\sigma}_{CR}$ is the mean of the count rate errors. If *S/N* is high (*S/N*>>1), the signal prevails over noise, while in the opposite case, the observed variations are dominated by the observational noise.

I used equation (7) to compute the *S/N* ratio for the lightcurves of all Seyfert galaxies in the SyI and SyII samples. Figure (3.1) shows the plot of σ^2_{NXV} as function of *S/N* of all sources. The horizontal blue solid line shows the line with σ^2_{NXV} =0, and the vertical blue dashed line shows the line with *S/N* =0.8. There are three sources that are beyond the boundaries of the plot. Two of them have the lowest *S/N* (*S/N* =0.2, with σ^2_{NXV} = -5.8 and σ^2_{NXV}=21.2), while the third one is the source with the highest *S/N* (*S/N* =38, and σ^2_{NXV} =0.084). Figure (3.1) shows that the scatter of the σ^2_{NXV} values when *S/N* >1 is way smaller than the scatter of σ^2_{NXV} at smaller *S/N*.

According to Allevato et al. (2013), the distribution of the σ^2_{NXV} measurements of a source is affected by its *S/N* ratio. As the *S/N* increases the variance of the σ^2_{NXV} distribution increases. This can explain why the scatter of the σ^2_{NXV} values is very large at low *S/N* ratio in Fig.(3.1). In this case, a single measurement of the σ^2_{NXV} does not provide a valid estimation of the intrinsic σ^2_{NXV}. Figure (3.1) also shows that the sample σ^2_{NXV} can take negative values, especially for cases with low *S/N* ratio. This can happen when the variability caused by the Poisson noise is comparable or larger than the intrinsic variability process.
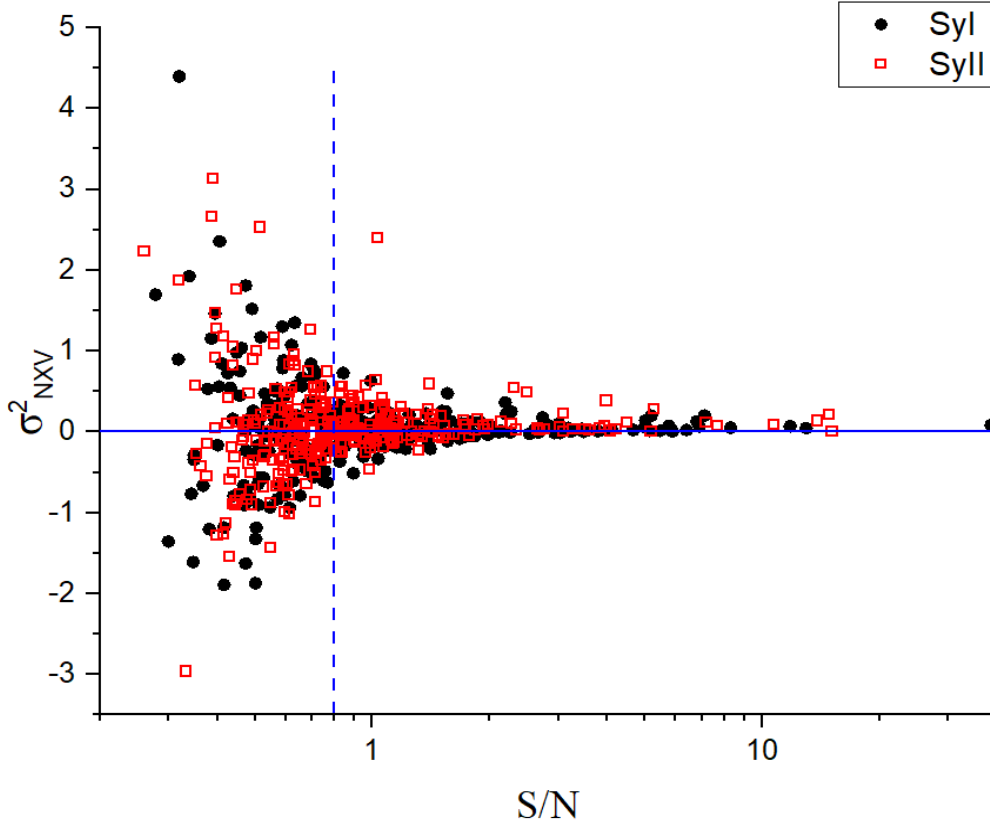
Figure 3.1 *Plot of σ^2_{NXV} as a function of S/N. Black filled dots correspond to SyI and red empty boxes correspond to SyII. The horizontal blue solid line shows the σ^2_{NXV} =0. The vertical blue dashed line shows the S/N =0.8.*

Taking all that into account, I follow Paolillo et al. (2017), and I chose to keep the sources with signal-to-noise ratio more than 0.8 (*S/N*>0.8), in order to avoid using measurements with large uncertainty.

3.2) The excess variance- time dependence

The normalized excess variance of the X-ray lightcurves of AGN depends on their time duration. The long timescale variations have large amplitude, while variations on shorter timescales have smaller amplitudes. This can be seen just by looking at the observed lightcurves. So the values of σ^2_{NXV} are expected to increase with time too.

Almost all the lightcurves at *105-Sbs* have a time duration, *T*, of 105 months. In the SyI and SyII samples there are a few exceptions, mentioned above, with a duration of 104 and 103 months. The duration, *T*, is measured in the observer's frame. However the sources in *105-Sbs* have different redshift, so the time duration is different in the rest frame of each one. I compute it using the following formula:

$$T_i = \frac{T_0}{1+z} \quad , \qquad (8)$$

where T_0 is the duration in the observer's frame, T_i is the duration in the rest frame of the source, and z is the redshift of the source.

What I wish to do is to compute the normalized excess variance using lightcurves that have the same time duration in rest frame for each source in both SyI and SyII samples. The highest z in both samples, belongs to a source named 2MASXJ23013626-5913210 (z =0.149). Using eq. (8) I estimate that the duration of the 105 BAT lightcurve in rest frame of this source is: $T_i(z=0.149)=91$ months. As I mentioned in section (2.6), the bin size of the BAT lightcurves, Δt, equals to one month (in the observer's frame). One month in the rest frame of a source, according to eq. (8) is: $\Delta t_i=1\,month/(1+z)$ So if I keep:

$$N_{new}=91(1+z) \quad , \qquad (9)$$

points in the lightcurve of each source, then the duration T_i of the lightcurve in the rest frame, combining the eq. (8) and eq. (9), will be:

$$T_i=N_{new}\Delta t_i=91(1+z)\cdot 1\,month/(1+z)=91 \quad months.$$

I used the new lightcurves and I re-computed the normalized excess variance for each source in the SyI and SyII samples. These are the σ^2_{NXV} values I will use from now on.

3.3) The S/N >0.8 samples

Initially, there were 370 and 448 sources in the SyI and SyII samples, respectively. After I decided to keep sources with $S/N>0.8$, these numbers changed. There are now 159 and 151 galaxies, in the SyI and SyII samples. These are the samples I will use from now on. For this reason, I computed again the distribution of F_{14-195} and z for the Seyferts in the new samples, in order to investigate whether they have similar properties or not, just like in section (2.4).
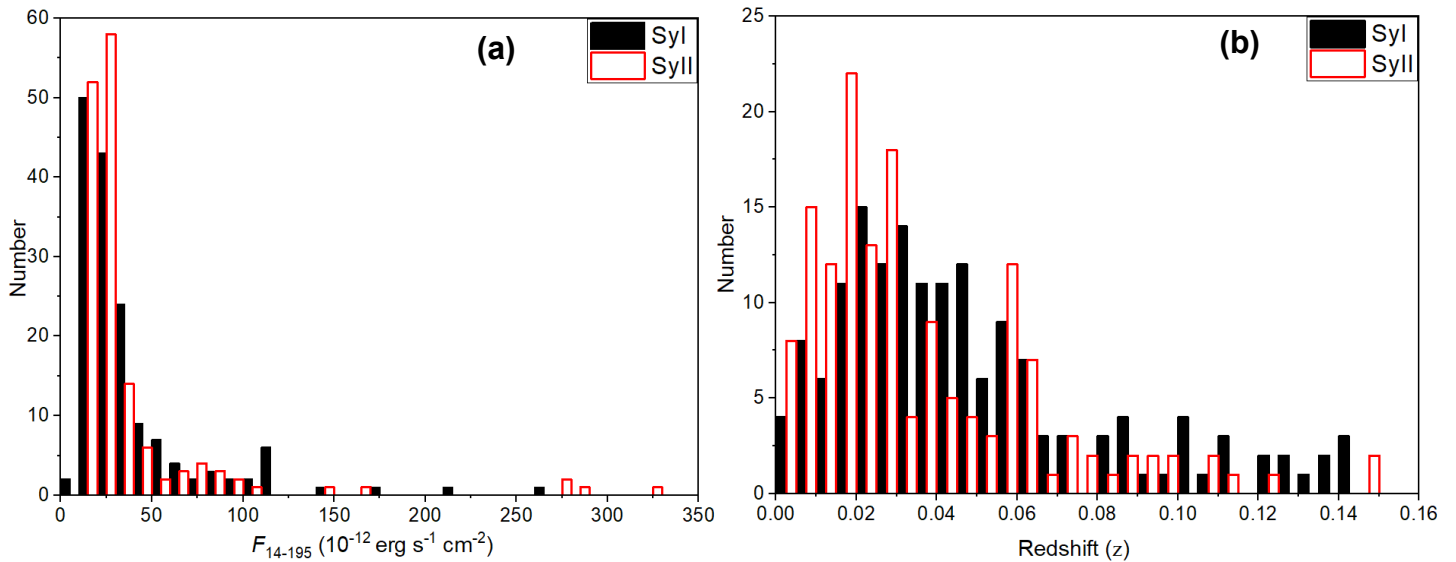
Figure 3.2 *Sample distribution of the* F_{14-195} *and redshift z (panel a and b respectively),using the sources with S/N>0.8. Black filled bars correspond to SyI and red open bars to SyII sources.*

Figure (3.2) shows the histograms of F_{14-195} and z of the Seyfert galaxies with $S/N>0.8$. Black filled bars show the distribution of the SyI data and red open bars show the distribution of the sources in SyII. As before, I used the K-S test to compare the distributions. Regarding F_{14-195}, the distribution of the new SyI and SyII samples, with $S/N>0.8$, appear to be similar to the previous F_{14-195} distributions in Fig. (2.3a). The results of the K-S test are $D_F = 0.11$ and $p_{null,F} = 0.31$. Since $p_{null,F}= 31\%$, I conclude that the F_{14-195} distributions of the SyI and SyII samples are drawn from the same distribution. For the z distributions, the results for the K-S

test are as follows: D_z = 0.25 and $p_{null,z}$ = 9.99 10^{-5}, therefore the two distributions are different. The conclusions are the same as before. The SyI distribution of redshift is systematically shifted to higher values, compared with the SyII redshift distribution, as shown by the histograms plotted in the right panel of Fig. (3.2).

3.4) The σ^2_{NXV} and Luminosity distributions

Left panel of Fig. (3.3) shows the sample distribution of σ^2_{NXV} for the SyI and SyII samples. Black filled bars correspond to SyI sources and red open bars to SyII sources. Figure (3.3**a**) shows that the distribution for SyIIs appears to be shifted to the right, when compared with the SyI distribution. In order to investigate whether the distributions are similar or not, I calculated the mean and median for the SyI and SyII samples and performed the K-S test. The results are presented in Table (3.1) and Table (3.2). The mean, and the median σ^2_{NXV} of the SyII sample is larger than the mean and median σ^2_{NXV} of the SyI sample. It seems like the SyII galaxies are more variable than the SyI galaxies. However, according to the K-S test results (D_σ^2 =0.17 and $p_{null,\sigma}^2$ =0.016), the difference between the two distributions is not statistically significant.

Right panel of Fig. (3.3) shows a plot of σ^2_{NXV} as function of z. Black filled dots represent SyI and red empty boxes represent SyII sources. There are two points that are not included in this plot: one with σ^2_{NXV} =2.1956 and z =0.047 and another one with σ^2_{NXV} =-0.904 and z =0.049. At low redshifts (z <0.01) the SyII sources prevail while for higher redshifts, (z >0.1) there are more SyI sources. The intermediate redshifts (0.01< z <0.1) the scatter of σ^2_{NXV} appears to be similar for both samples. This plot as well the K-S test results distribution of σ^2_{NXV} for the SyI and SyII samples, indicate that the variability properties of the two samples are not very different.
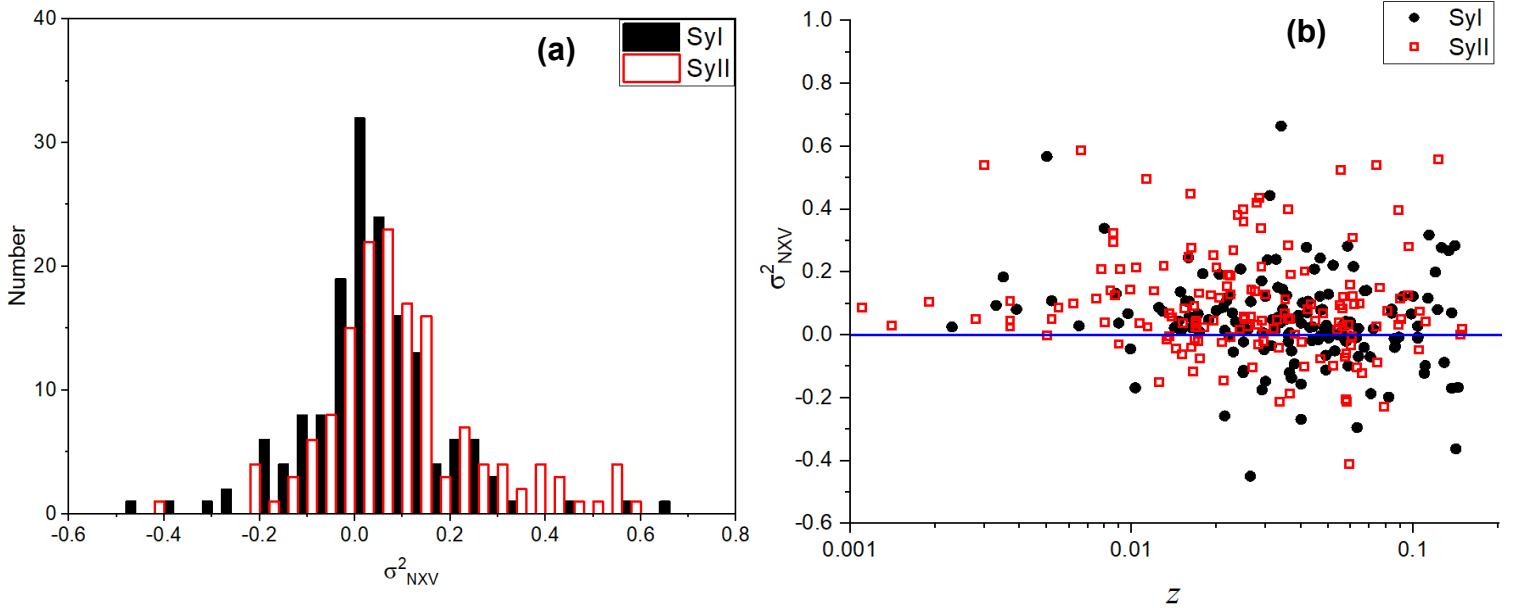
Figure 3.3 *Left panel (**a**) shows the sample distribution of σ^2_{NXV} . Black filled bars correspond to SyI sources and red open bars to SyII sources. Right panel (**b**) shows the a of σ^2_{NXV} as function of z (black filled dots represent SyI and red empty boxes represent SyII). The blue solid line indicates σ^2_{NXV}=0. The x axis is in logarithmic scale.*

As I have discussed in the introduction, the excess variance correlates with X-ray luminosity in AGN. I will use the values of σ^2_{NXV} calculated from the lightcurves in *105-Sbs* and the luminosity values listed in Table 1 of Baumgartner et al. (2013) (https://iopscience.iop.org/article/10.3847/1538-4365/aa96ad), to investigate this issue. Ricci et al. (2017), in their section (5.1), describe how they calculated the luminosity in the 14-195 keV band. They used the following formula:

$$L_{14-195} = 4\pi d_L^2 \frac{F_{14-195}}{(1+z)^{2-\Gamma}} \quad , \qquad (10)$$

where F_{14-195} is the flux in the 14-195 keV band, d_L is the cosmology-corrected (H_0 =70 km/sec/Mpc, Ω_{matter} =0.3, Ω_{vacuum} =0.7) luminosity distance (for some sources with z <0.01 d_L is the redshift-independent distance), z is the redshift and Γ is the photon index obtained by fitting the Swift BAT spectra with a single power-law model. Two sources in the sample, (IGR J16385-2057 and 2MASX J13032223-1341332) were not included in Ricci et al. (2017) so I computed their L_{14-195} as follows:

$$L_{14-195} = F_{14-195}\, 4\pi d_L^2 \quad , \qquad (11)$$

where d_L is the cosmology-corrected luminosity distance, same as above, taken from NED: (http://ned.ipac.caltech.edu/).

Figure (3.4) shows the sample distribution of the logarithm L_{14-195}, $log(L_{14-195})$, of the Seyfert galaxies in the *105-SBc* with *S/N*>0.8. Black filled bars correspond to SyI sources and red open bars to SyII sources. I calculated the mean and median for the SyI and SyII samples. The results are listed in Table (3.1). The difference between the mean and median $log(L_{14-195})$ of the two samples is ~0.3. This implies that, on average, SyI sources are twice as luminous than SyII sources. This is in agreement with Fig. (3.4), which shows that there are more SyI sources at large $log(L_{14-195})$ values, while SyII prevail in number at lower $log(L_{14-195})$. The results of the K-S test are: D_L =0.22 and $p_{null,L}$ =0.0007, which indicate that, statistically speaking, the two distributions are significantly different.
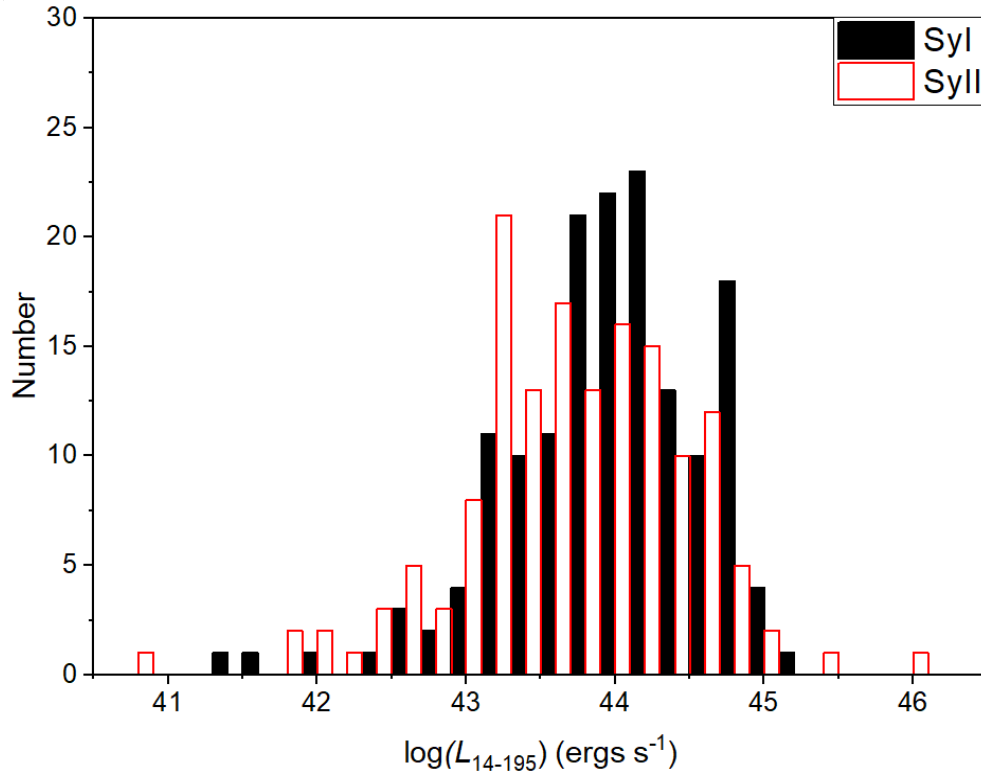
Figure 3.4 *Sample distribution of log(L_{14-195}). Black filled bars correspond to SyI sources and red open bars to SyII sources.*

As I discussed, the F_{14-195} distributions of the SyI and SyII samples are similar but the z and $log(L_{14-195})$ distributions are different. As a consequence of the z distributions being different, the distance distributions of SyI and SyII samples should also differ. The SyI sample should be systematically shifted to higher distances, compared with the SyII sample. According to equation (10) if the flux distributions of the two samples are the same but the SyI sources are more distant, then the luminosity distributions (i.e. the $log(L_{14-195})$ distributions) of the SyI and SyII samples much also be different. The SyI sources shall be brighter than the SyII sources. That explains the results discussed above.

Type	$\overline{\sigma^2}_{NXV}$	$log(\overline{L}_{14\text{-}195})$
Sy I	0.038 (0.031)	43.95 (44.00)
Sy II	0.107 (0.057)	43.68 (43.69)

Table 3.1: Mean and median (values in parenthesis) for the distribution of σ^2_{NXV} and $log(L_{14\text{-}195})$ of the SyI and SyII samples.

D_F	$p_{null,F}$	D_z	$p_{null,z}$	$D\sigma^2_{NXV}$	P_{null,σ^2}	D_L	$p_{null,L}$
0.11	0.31	0.25	$9.99\ 10^{-5}$	0.17	0.016	0.22	0.0007

Table 3.2: Kolmogorov-Smirnov test results, the K–S statistic D and the probability p_{null} for the distribution of $F_{14\text{-}195}$, z, σ^2_{NXV} and $log(L_{14\text{-}195})$ of the SyI and SyII galaxies.

3.5) The log(M_BH) and accretion rate distributions

I retrieved the black hole masses values for the sources in the SyI and SyII sample from Koss et al. (2017). I used the following values in priority order:

1) For 30 sources I chose the *log(M_BH)* estimate from Bentz & Katz (2015), (http://www.astro.gsu.edu/AGNmass/), which are calculated based on the reverberation method.

2) $\log\left(M_{BH,\sigma.}\right)$, from Table 4, for 72 AGN with reliable measurements of stellar velocity dispersion, σ_* , Koss et al. (2017) used the relation from Kormendy & Ho (2013):

$$\log\left(\frac{M_{BH,\sigma.}}{M_\odot}\right) = 4.38\log\left(\frac{\sigma_*}{200\,km\,s^{-1}}\right) + 8.49 \quad .$$

3) $M_{BH}(H\beta)$ from Table 9, for 102 sources with broad Hβ lines Koss et al. (2017) used the prescription of Trakhtenbrot & Netzer (2012):

$$M_{BH}(H\beta) = 1.05\cdot10^8 \left(\frac{L_{5100}}{10^{46}\,erg\,s^{-1}}\right)^{0.65} \cdot \left(FWHM\,\frac{(H\beta)}{10^3\,km\,s^{-1}}\right)^2 M_\odot \quad ,$$

where L_{5100} is the monochromatic luminosity at rest-frame 5100 Å, and *FWHM(Hβ)* is measured from the entire (best-fit) broad profile.

4) $M_{BH}(H\alpha)$ (Table 9), for 6 sources with broad *Hα* lines. Koss et al. (2017) used the prescription of Greene & Ho (2005):

$$M_{BH}(H\alpha) = 1.3\cdot10^6 \left(\frac{L_{H\alpha}}{10^{42}\,erg\,s^{-1}}\right)^{0.57} \cdot \left(FWHM\,\frac{(H\alpha)}{10^3\,km\,s^{-1}}\right)^2 M_\odot \quad ,$$

where $L_{H\alpha}$ is the integrated luminosity of the broad component of the Hα line, determined from the best-fitting model.

5) *log(M_BH,lit)* (Table 4), for 3 sources with *log(M_BH)* computed through the $\log\left(M_{BH}\right) - \sigma_*$ relation, with σ_* from literature.

In total I managed to find the *log(M_BH)* estimates for 213 out of 310 sources in the original sample (~68.7% of the total). There are 136 sources out of 159 in the SyI sample and 77 sources out of 151 in the SyII sample

Figure (3.5) shows the *log(M_BH)* distribution for the SyI and SyII sources. Black filled bars correspond to SyI sources and red open bars to SyII sources. In general the SyII sources tend to have higher values of *log(M_BH)* than the SyI sources. I used the K-S test in order to test if the two distributions differ. The results are: D_M =0.35 and $p_{null,M}$ =9.64 10^{-6}, so the two distributions are significantly different. That may be due to the fact that SyII galaxies need to be brighter in order to be detected by the *Swift*-BAT, because of the absorption, which affects their X-ray spectrum. As I mention in the introduction sources with large black hole mass should have high values of luminosity.
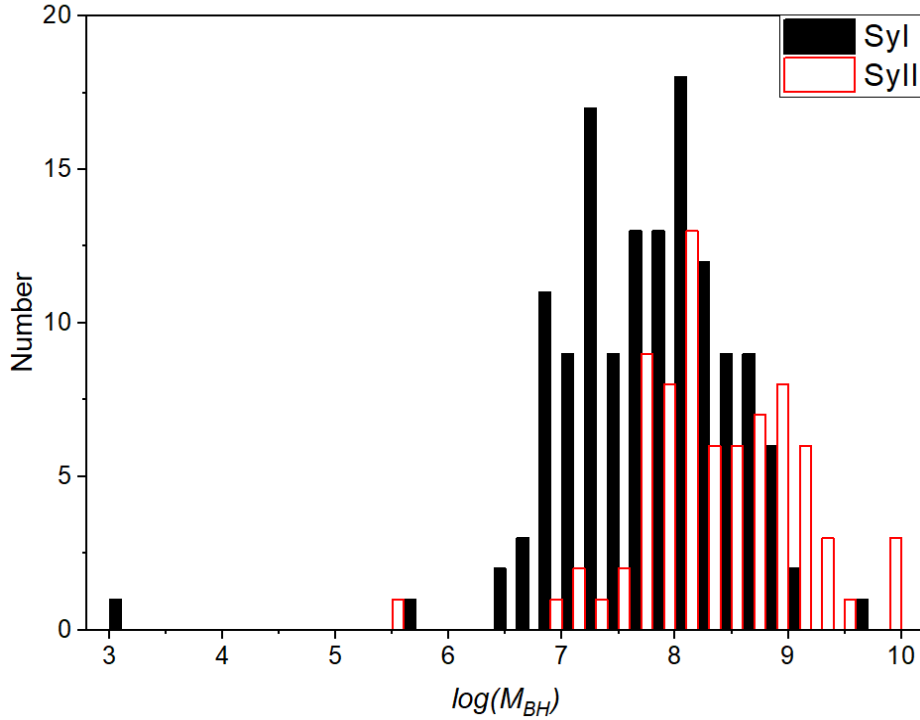
Figure 3.5 *Distribution of log(M_BH). Black filled bars correspond to SyI sources and red open bars to SyII sources.*

Finally, I calculated the accretion rate of the objects with known M_{BH}. As I mention in the introduction, AGN are powered by the gravitational energy released of matter accreting onto the central black hole. This process can convert the mass, M, of an object into energy, E, with efficiency, η , of ~5 to over 40 percent, depending on whether the Black Hole is spinning or not. So, the bolometric luminosity of an AGN is given by: $L_{bol} = \eta \dot{M} c^2$, where $\dot{M}$ is the accretion rate. The outward pressure of the radiation needs to balance the inward gravitational force to sustain the mass accretion. This means that the luminosity must not exceed the so called Eddington luminosity, which is defined as:

$$L_{Edd} = \frac{4 \pi G M m_p c}{\sigma_T} \simeq 1.25 \times 10^{38} \left(\frac{M}{M_\odot} \right) erg \, s^{-1} \quad .$$

The Eddington accretion rate is defied via the relation: $L_{Edd} = \eta \dot{M}_{Edd} c^2$. If $L_{14\text{-}195}$ is representative of the bolometric luminosity, i.e. $L_{bol} \propto L_{14-195}$, then $\dfrac{L_{14-195}}{M_{BH}}$ should be proportional to $\lambda_{Edd} \equiv \dfrac{\dot{M}}{\dot{M}_{Edd}}$, since:

$$\lambda_{Edd} = \frac{\dot{M}}{\dot{M}_{Edd}} \propto \frac{\dfrac{L_{14-195}}{\eta c^2}}{\dfrac{L_{Edd}}{\eta c^2}} = \frac{L_{14-195}}{\dfrac{1.25 \times 10^{38}}{M_\odot} M_{BH}} \Rightarrow \lambda_{Edd} \propto \frac{L_{14-195}}{M_{BH}} \quad .$$

Therefore, the quantity $\dfrac{L_{14-195}}{M_{BH}}$, or $\log(L_{14-195}) - \log(M_{BH})$,should be proportional to the

$\log(\lambda_{Edd}) = \log\left(\dfrac{\dot{M}}{\dot{M}_{Edd}}\right) \propto \log(L_{14-195}) - \log(M_{BH})$ for the objects with known M_{BH}, in the SyI and SyII sample. Hereafter I will call the quantity $\log(L_{14-195}) - \log(M_{BH})$ as the "accretion rate", for simplicity.

Figure (3.6**a**) shows the sample distribution of the accretion rate for the SyI and SyII sample. It shows that the accretion rate of the SyI sources is larger than the SyII sources. The results for the K-S test are: $D_{\dot{m}} = 0.68$ and $p_{null,\dot{m}} = 1.21 \cdot 10^{-20}$, so the two distributions are significantly different.

For reasons that will become clear in the next chapter, I constructed a sample of SyI and SyII sources with the same accretion rate distribution. Figure (3.6**b**) shows the two distributions of SyI and SyII samples with accretion rate between 34 and 35.8 (87 sources). The two distributions are similar. The K-S test results ($D_{\dot{m}} = 0.31$ and $p_{null,\dot{m}} = 0.046$) confirm the above statement. I will examine if the sample distributions of σ^2_{NXV}, for those 87 sources are similar too. Figure (3.7) shows the sample distribution of σ^2_{NXV} for these sources. I also used the K-S test in order to test if the two distributions differ. The results are: $D_\sigma^2 = 0.24$ and $p_{null,\sigma^2} = 0.22$, which indicates that the σ^2_{NXV} distributions of the SyI and SyII samples for those sources are drawn from the same distribution.
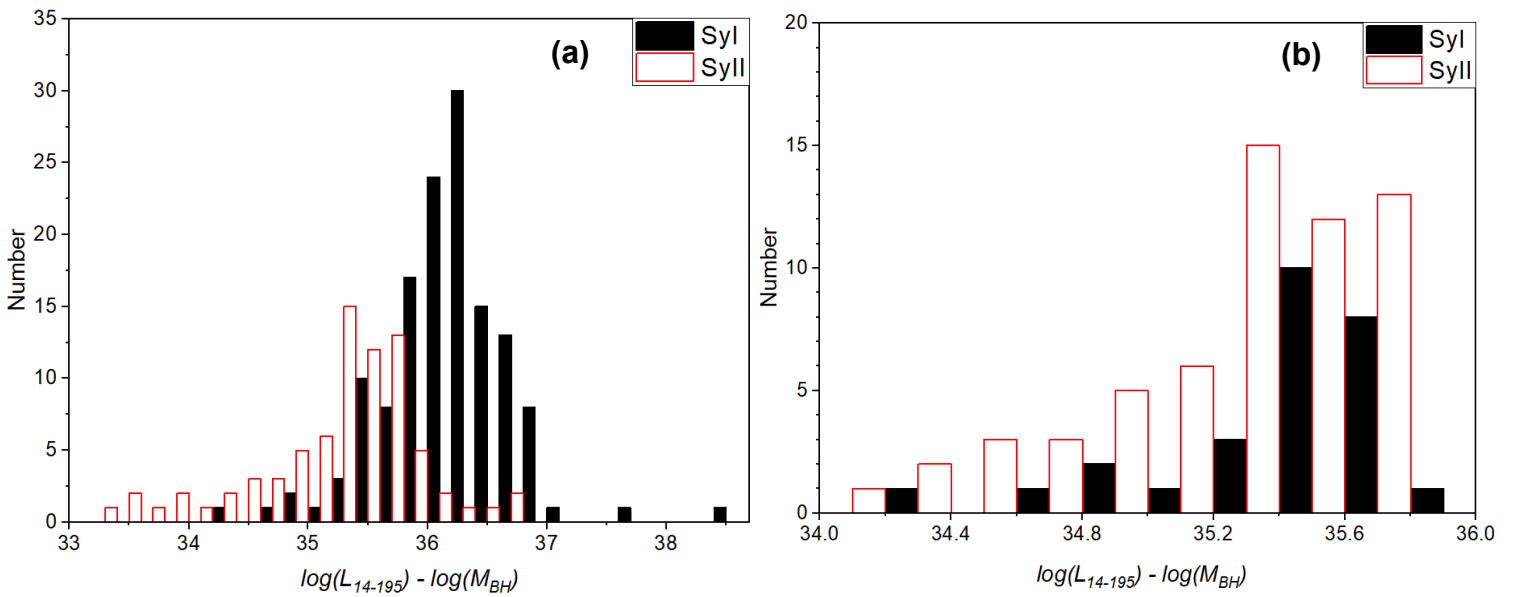
Figure 3.6 *Left panel (**a**) shows the sample distribution of accretion rate for all the 213 sources. Black filled bars correspond to SyI sources and red open bars to SyII sources. Right panel (**b**) shows the sample distribution of accretion rate for the 87 sources, with accretion rate between 34 and 35.8. Black filled bars correspond to SyI sources and red open bars to SyII sources.*
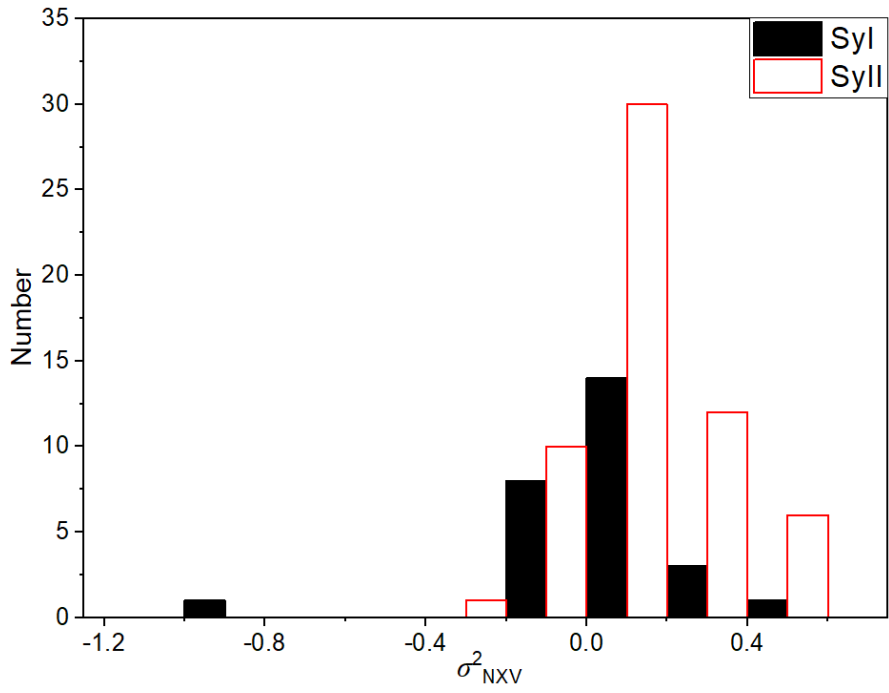
Figure 3.7. *Distribution σ^2_{NXV} for accretion rate for the 87 sources, with accretion rate between 34 and 35.8. Black filled bars correspond to SyI sources and red open bars to SyII sources.*

CHAPTER 4. RESULTS

4.1) The dependence of σ^2_{NXV} on Luminosity

The main object of this chapter is to examine the correlation between σ^2_{NXV} and other observational propetries, such as $log(L_{14-195})$ and $log(M_{BH})$ in the SyI and SyII sample. Figure (4.1) shows a plot of σ^2_{NXV} vs $log(L_{14-195})$, for the SyI and SyII samples. Black circles represent SyI sources and red boxes represent SyII sources. Figure(4.1) does not provide much information, regarding the dependence of σ^2_{NXV} to luminosity due to the large scatter. Nevertheless, the lack of negative measurements for values below $log(L_{14-195})$ =43 is noticeable. This implies that the low-luminosity sources are more variable, but we cannot conclude many more.
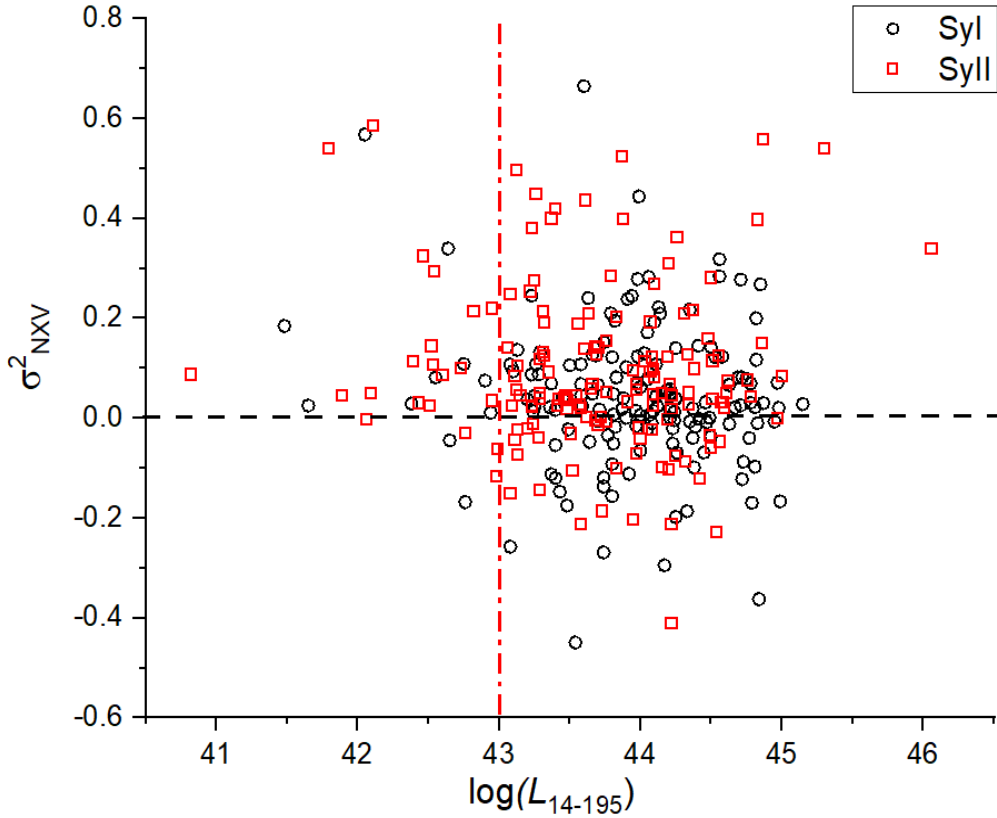
Figure 4.1. *Plot of σ^2_{NXV} as function of $log(L_{14-195})$. Black circles represent SyI sources and red squares represent SyII sources. Black dashed line shows the value $\sigma^2_{NXV}=0$. Red dashed line shows the value $log(L_{14-195})=43$.*

In order to reduce the scatter in Fig(4.1), I will bin the data. To do so, I ordered the σ^2_{NXV} measurements in ascending order of $log(L_{14-195})$. Then I calculated the mean σ^2_{NXV} and $log(L_{14-195})$, and their error, in various bins, using the following formulas:

$$\bar{M} = \frac{1}{N} \sum_{i=1}^{N} m_i \quad , \qquad (12)$$

$$\delta_{\bar{M}} = \sqrt{\frac{1}{N(N-1)} \sum_{i=1}^{N} (m_i - \bar{M})^2} \quad , \qquad (13)$$

where $\bar{M}$ and $\delta_{\bar{M}}$ are the mean and its error in each bin, and N is the number of measurements, m_i, in each bin. I divided the SyI and SyII data in three bins with, $N=50$ and $N=59$ for the first two and for the third bin of the SyI sample, and $N=50$ and $N=51$ for the first two and for the last bin of the SyII sample.

Then, I calculated the logarithm of the mean σ^2_{NXV}, $\log(\overline{\sigma^2}_{NXV})$ and the corresponding error value using the law of propagation of uncertainty:

$$\delta f^2 = \left(\frac{\partial f}{\partial a_1}\delta\alpha_1\right)^2 + \left(\frac{\partial f}{\partial a_2}\delta\alpha_2\right)^2 + \ldots + \left(\frac{\partial f}{\partial a_n}\delta\alpha_n\right)^2 . \qquad (14)$$

In our case:

$$\delta_{\log\overline{\sigma^2}} = \sqrt{\left(\frac{\delta_{\overline{\sigma^2}}}{\overline{\sigma^2}_{NXV}\ln 10}\right)^2} .$$
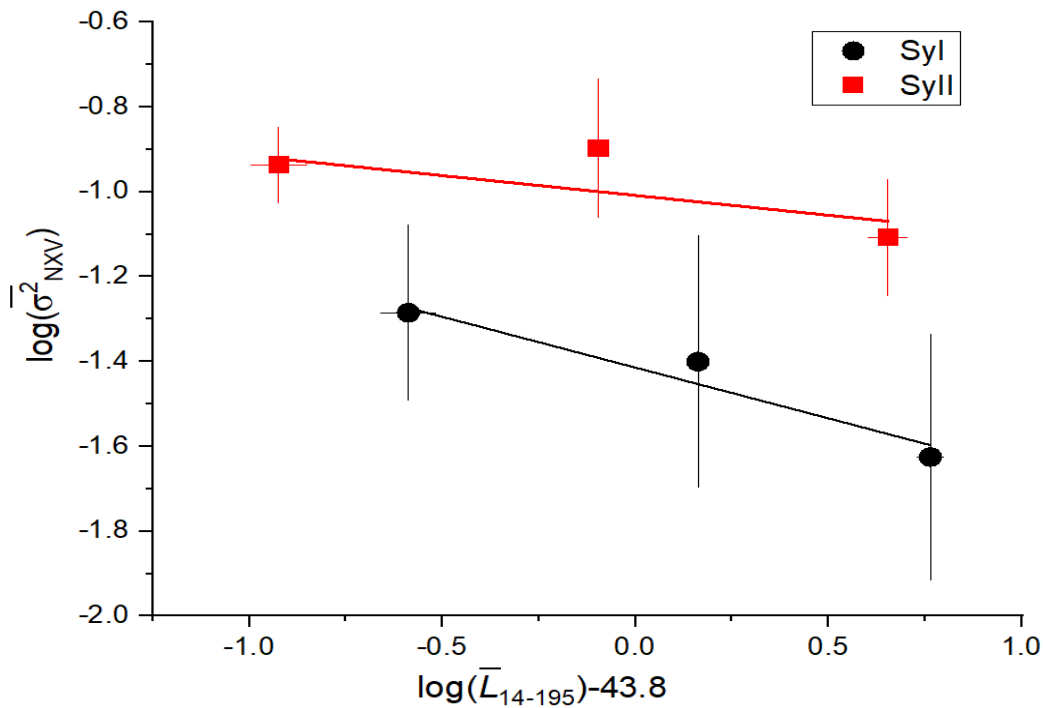
Figure 4.2. *Plot of mean values, calculated per ~50 points, of log(σ^2_{NXV}) as a function of log(L_{14-195}) for the SyI and SyII samples separately. Black dots and black line represent the SyI sample, while red squares and red line represent the SyII sample. Solid lines represent the best linear fit, using the method of linear least squares.*

Figure (4.2) shows the plot of the binned measurements of $\log(\overline{\sigma^2}_{NXV})$ vs $\log(\overline{L}_{14-195})$. Black dots represent the SyI sample, while red squares represent the SyII sample. By the looks of it, σ^2_{NXV} appears to depend on *log(L_{14-195})*. Mostly for the SyI sources, σ^2_{NXV} arrears to decrease as the *log(L_{14-195})* increases. In addition, the SyII sources have noticeably higher values of σ^2_{NXV} than the SyI sources for the same values of *log(L_{14-195})*. In order to quantify the correlation between σ^2_{NXV} and *log(L_{14-195})* I fitted the data in Fig. (4.2) with a linear model of the following form:

$$\log(\overline{\sigma^2}_{NXV}) = a + b[\log(\overline{L}_{14-195}) - 43.8] , \qquad (15).$$

where 43.8 is the mean of the *log(L_{14-195})* distribution, for the SyI and SyII samples combined. I used $\log(\overline{L}_{14-195}) - 43.8$, instead of just $\log(\overline{L}_{14-195})$, to minimize the error of the intercept, α. In this case the value of α is given at *log(L_{14-195})* =43.8, not at *log(L_{14-195})* =0, which is far from the range of value in this sample.

I applied the method of linear least squares, as described below, in order to calculate the intercept and slope for the SyI and SyII data separately. Mathematically, the linear least squares best-fit method is used for estimating the unknown parameters in a linear regression model, $y = a + bx$. This method gives the values of a and b when the distance between the corresponding curve, $y = a + bx$, and the experimental points, $(x_i, y_i \pm \sigma_i)$, is minimized. When taking into account the errors on the y-axis, and assuming the values on x-axis are known exactly, we measure the distance between data and model fit using the chi-square function:

$$\chi^2(a, b) = \sum_{i=1}^{N} \left(\frac{y_i - a - bx_i}{\sigma_i} \right)^2 . \qquad (16)$$

The model which provides the best fit to the data is the one when χ^2 is minimized, thus the best fit values of a and b are calculated from $\frac{\partial \chi^2}{\partial a} = 0$ and $\frac{\partial \chi^2}{\partial b} = 0$. So

$$a = \frac{1}{\Delta} \left(\sum \frac{x_i^2}{\sigma_i^2} \sum \frac{y_i}{\sigma_i^2} - \sum \frac{x_i}{\sigma_i^2} \sum \frac{x_i y_i}{\sigma_i^2} \right), \sigma_\alpha = \sqrt{\frac{1}{\Delta} \sum \frac{x_i^2}{\sigma_i^2}} , \qquad (18)$$

and

$$b = \frac{1}{\Delta} \left(\sum \frac{1}{\sigma_i^2} \sum \frac{x_i y_i}{\sigma_i^2} - \sum \frac{x_i}{\sigma_i^2} \sum \frac{y_i}{\sigma_i^2} \right), \sigma_b = \sqrt{\frac{1}{\Delta} \sum \frac{1}{\sigma_i^2}} , \qquad (19)$$

where,

$$\Delta = \sum \frac{1}{\sigma_i^2} \sum \frac{x_i^2}{\sigma_i^2} - \left(\sum \frac{x_i}{\sigma_i^2} \right)^2 . \qquad (20)$$

Black and red lines in Fig. (4.2) show the best fit lines of the SyI and SyII data respectively. The best fit results are listed in Table (4.1). The bottom row in Table (4.1) lists the difference between the best-fit intercepts, α, and slopes, b, for the SyI and SyII data. The results for the slopes, b, indicate that the slope, is probably the same for the SyI and SyII data as the difference is just ~1.5σ away from zero. Therefore σ^2_{NXV} has similar dependence on $log(L_{14-195})$ for both SyI and Sy II sample: σ^2_{NXV} tends to decrease with increasing $log(L_{14-195})$. The weighted mean slope is calculated via the formula:

$$\bar{b} = \frac{\frac{b_{SyI}}{\sigma^2_{b_{SyI}}} + \frac{b_{SyII}}{\sigma^2_{b_{SyII}}}}{1/\sigma^2_{b_{SyI}} + 1/\sigma^2_{b_{SyII}}}$$

and the corresponding error:

$$\sigma^2_{\bar{b}} = \frac{1}{1/\sigma^2_{b_{SyI}} + 1/\sigma^2_{b_{SyII}}} .$$

The results for slope are: $\bar{b} = -0.15 \pm 0.09$, which indicates a slope that is significantly different than zero.

However, the intercept, α, is significantly different for the two samples. In fact, α_{SyII} is significantly larger than α_{SyI}. So, the SyII sources are more variable than the SyI sources. Actually this agrees with the appearance of the σ^2_{NXV} distribution shown in Fig. (3.3).

$log(\overline{\sigma^2}_{NXV}) = \alpha + b[log(\overline{L}_{14-195}) - 43.8]$		
	α	b
SyI	-1.41±0.03	-0.24 ±0.05
SyII	-1.01±0.06	-0.09±0.07
Δ(SyII-SyI)	0.41±0.06	0.15±0.09

Table 4.1: Best fit results to the data plotted in Fig.(4.2). Δ(SyII-SyI) indicates the difference between the best fit values.

4.2) The dependence of σ^2_{NXV} on the black hole mass

In this subsection, I will examine the correlation between σ^2_{NXV} and *log(M$_{BH}$)*. I used the same SyI and SyII samples for *log(M$_{BH}$)*, that I defined in sub-section (3.5). Figure (4.3) shows the plot of σ^2_{NXV} as function of the *log(M$_{BH}$)*. Black circles represent SyI sources and red boxes represent SyII sources. The scatter is large, just like in Fig. (4.1), and as a result this plot does not provide much information on its own.
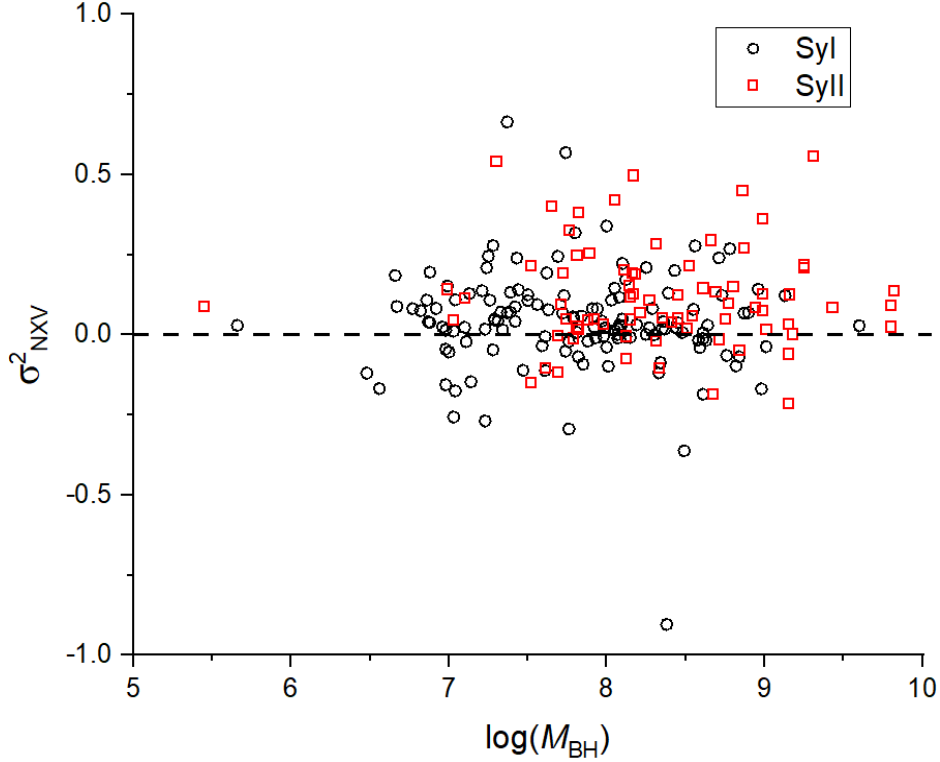
Figure 4.3. *Plot of σ^2_{NXV} as function of log(M$_{BH}$). Black circles represent SyI sources and red squares represent SyII sources. Black dashed line shows the σ^2_{NXV}=0.*

I followed the same process as before, to bin the data. I ordered the sources in ascending order of *log(M$_{BH}$)*, and calculated the σ^2_{NXV} and *log(M$_{BH}$)* mean and their error, using eq.(12) & (13). N=40 and N=56 for the first two and the last bin in the SyI sample, while N=40 and N=37 for the first and second bin in SyII sample. Then, I calculated the logarithm of $\log\left(\overline{\sigma^2}_{NXV}\right)$ and the corresponding error value using the law of propagation of uncertainty i.e. eq.(14).

Figure (4.4) shows a plot of $\log\left(\overline{\sigma^2}_{NXV}\right)$ vs $\log\left(\overline{M}_{BH}\right)$. Black dots represent the SyI sample, while red squares represent the SyII sample. Once again I fitted the points of $\log\left(\overline{\sigma^2}_{NXV}\right)$ and $\log\left(\overline{M}_{BH}\right)$, for the SyI data only, in order to quantify their correlation, with a linear model of the following form:

$$\log\left(\overline{\sigma^2}_{NXV}\right)=a+b\left[\log\left(\overline{M}_{BH}\right)-8\right] \quad , \qquad (21).$$

where 8 is the mean of the *log(M$_{BH}$)* distribution. I used $\log\left(\overline{M}_{BH}\right)-8$ instead of $\log\left(\overline{M}_{BH}\right)$ for the same reason as before. I did not applied the linear fit to SyII data, because there are only two points in Fig. (4.4) for the SyII sample.

I applied the method of linear least squares, in order to compute the intercept α and slope b for the SyI data. The results are as follows: $b=0.1\pm0.5$, and, $a=-1.2\pm0.2$. The black line in Fig. (4.4) represent the best fit line to the SyI points. This line suggests that σ^2_{NXV} may increase with increasing *log(M$_{BH}$)*, but the error on *b* is large. Within 1σ the slope is consistent with $b=0$,so σ^2_{NXV} could be constant regardless

the *log(M$_{BH}$)*. It is also possible that $b<0$, which indicates that σ^2_{NXV} may decrease as the *log(M$_{BH}$)* increases.

In order to test if there are any differences between the two samples, I computed the distance between the best-fit function $\log(\overline{\sigma}^2_{NXV})=a+b[\log(\overline{M}_{BH})-8]$ and the SyII points in Fig. (4.4). The distance is given by: $D=\log(\overline{\sigma}^2_{NXV,SyII})-a+b[\log(\overline{M}_{BH})-8]$,   and   its   error   is: $\delta_D=\sqrt{\delta^2_{\log(\overline{\sigma}^2_{NXV,SyII})}+\delta^2_a+\delta^2_b(\log\overline{M}_{BH}-8)^2+b^2\delta^2_{\log\overline{M}_{BH}}}$ where $\delta_{\log(\overline{\sigma}^2_{NXV,SyII})}$ is the error of $\log(\overline{\sigma}^2_{NXV})$ for the SyII points, $\delta_a=0.2$, $\delta_b=0.5$ and $\delta_{\log(\overline{M}_{BH})}$ is the error of the mean black hole mass of SyI values. The results are as follows: for the point at (-0.21±0.08, -0.76±0.14), the distance is: $D_1=0.5\pm0.3$. For the point at (0.90±0.07, -0.97±0.10), the distance is: $D_2=0.1\pm0.5$. In both cases, the distance values are consistent with zero, which suggests that, statistically speaking, the SyII data are consistent with the $\log(\overline{\sigma}^2_{NXV})$ - $\log(\overline{M}_{BH})$ relation that I derived for the SyI data.
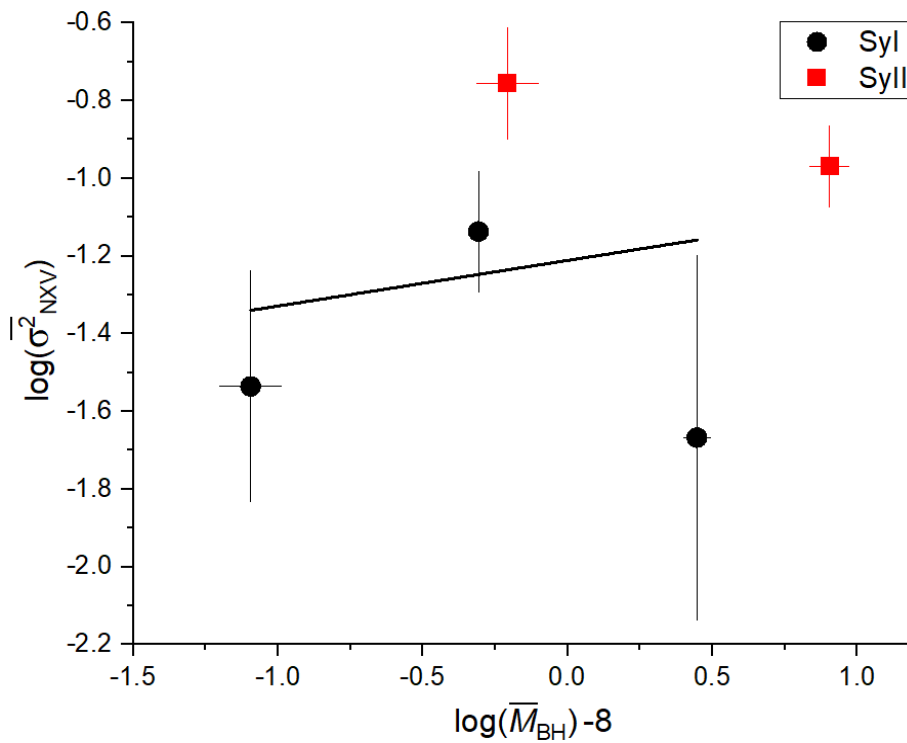
Figure 4.4. *Plot of mean log(σ²$_{NXV}$) vs log(M$_{BH}$), calculated per ~40 points, for the SyI and SyII samples separately. Black dots represent the SyI sample, while red squares represent the SyII sample. The black line represents the best linear fit, using the method of linear least squares for the SyI sample.*

CHAPTER 5. MODEL FITS OF THE σ^2_{NXV} -M_{BH} RELATION

As I disguised in Chapter 3, the σ^2_{NXV} may depend on the accretion rate in addition to BH mass. In order to construct a σ^2_{NXV} -M_{BH} relation, free of the accretion rate dependence, I used the sample of SyI and SyII sources with same accretion rate, that I discussed in section (3.5). For those sources, I calculated the mean and its error, using eqs.(12) & (13). I binned $\log\left(\overline{\sigma^2}_{NXV}\right)$ and $\log\left(\overline{M}_{BH}\right)$ per 20 points for the first three bins and for the third bin I used 26 points. Figure (5.1) shows the plot of $\log\left(\overline{\sigma^2}_{NXV}\right)$ vs $\log\left(\overline{M}_{BH}\right)$ for these sources.
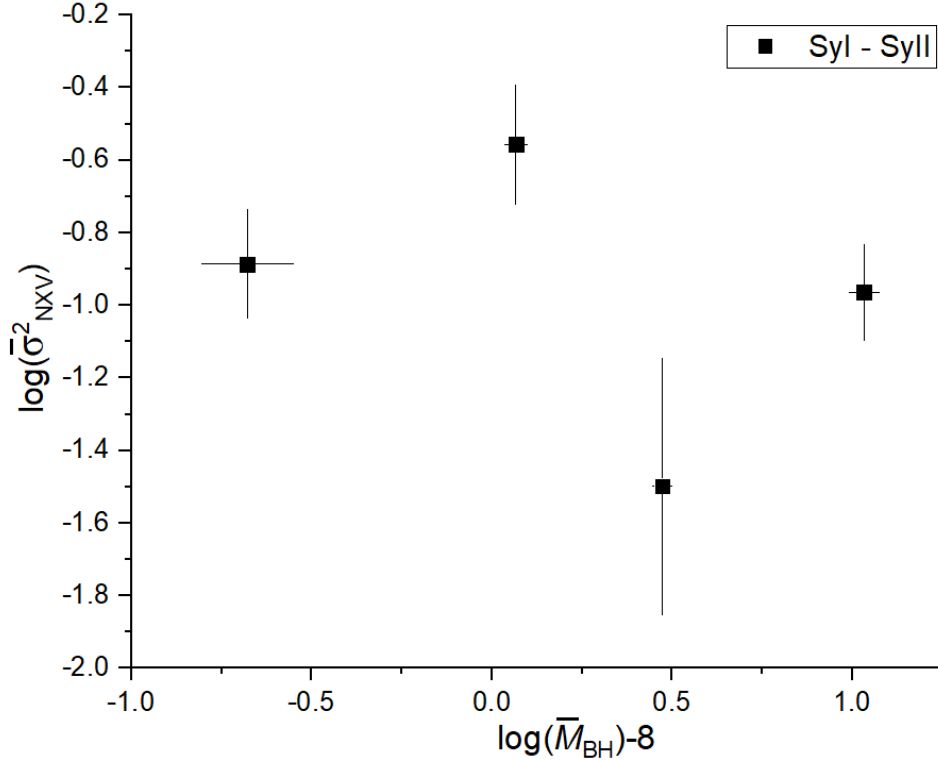
Figure 5.1 *Plot of log(σ^2_{NXV}) vs log(M_{BH}), calculated per ~20 points, for the SyI and SyII sources, with the same accretion rate.*

The power spectral density function, or simply power-spectrum, *PSD(v)*, is an important function that quantifies the variability properties of a random process. According to Fourier analysis, any variable process can be decomposed into a number of discrete sinusoidal components. In the case of a random, stationary process is defined in such a way that:

$$\sigma^2 = \int_0^\infty PSD(v)\,dv \quad , \qquad (22)$$

where σ^2 is the variance of the process. Equation (22) shows that $PSD(v)\,dv$ is equal to the contribution of the variability components, with frequency between v and $v+dv$, to the total variance of the process.

Allevato et al. (2013) have shown that σ^2_{NXV} of a lightcurve with bin size Δt, for a total period of time, T, is a measure of the intrinsic band-variance, defined as follows:

$$\sigma^2_{band} = \int_{v_{min}}^{v_{max}} PSD(v)\,dv \quad , \qquad (23)$$

where $v_{min} = \dfrac{1}{T}$ and $v_{max} = \dfrac{1}{\Delta t}$. For the BAT lightcurves in this work, v_{min}=3.6·10⁻⁹ Hz and v_{max}=3.8·10⁻⁷ Hz. Equation (23) can be used to model the σ^2_{NXV} - M_{BH} relation for the sources plotted in Fig. (5.1), as long as the $PSD(v)$ is known.

Estimation of the $PSD(v)$ is not easy, as it requires the use of long, uninterrupted lightcurves, which are not usually available, at least in X-rays. The $PSD(v)$ has been estimated in a few well observed, nearby AGN. The results have shown that $PSD(v)$ is well approximated by the following function (e.g. McHardy et al. (2004), Gonzalez-Martin & Vaughan (2012)):

$$PSD_{mod}(v) = A\,v^{-1}\left(1 + \frac{v}{v_b}\right)^{-1} , \qquad (24)$$

where v_b is the "break" or "bending" frequency, and A is the $PSD(v)$ amplitude: $A = 2 \times PSD(v_b) \times v_b$. Equation (24) shows that at low frequencies $(v \ll v_b)$, the $PSD(v)$ is proportional to v^{-1} , while at high frequencies $(v \gg v_b)$, $PSD(v) \propto v^{-2}$, i.e. the $PSD(v)$ follows a power-law shape with slope from -1 to -2, depending on the "break" frequency.

According to the model $PSD(v)$, as defined in eq. (24), eq. (23) transforms to:

$$\sigma^2_{mod} = \int_{v_{min}}^{v_{max}} PSD_{mod}(v)\,dv = A\left[\ln\left(\frac{v_{max}}{v_{min}}\right) - \ln\left(\frac{v_b + v_{max}}{v_b + v_{min}}\right)\right] . \qquad (25)$$

Equation (25) can be used to fit the observed σ^2_{NXV} - M_{BH} relation. In order to do that it is necessary to understand the dependence of A and v_b on M_{BH}. Based on the results from the $PSD(v)$ analysis of nearby AGN, v_b decreases with increasing M_{BH}, and it may also depend on luminosity, while the $PSD(v)$ amplitude may be constant or may depend on the accretion rate. Following Paolillo et al. (2017), I fitted the data shown in Fig. (5.1), assuming the following models:

i) Model 1: $A = constant$ and $v_b = 580/(M_{BH}/M_\odot)\,s^{-1}$. In this model the PSD amplitude is constant and the break frequency decreases as the M_{BH} increases.

ii) Model 2: $A = constant$ and $v_b = \dfrac{200}{86400}(L_{44,bol})(M_{6,BH})^{-2}\,s^{-1}$, where $L_{44,bol}$ is the bolometric luminosity in units 10⁴⁴ erg s⁻¹, and $M_{6,BH}$ is the BH mass in units 10⁶ $M_\odot$. The PSD amplitude is constant, as in Model 1, but the break frequency dependents on M_{BH} and on accretion rate too, via L_{bol} . The break frequency decreases with increasing M_{BH} and decreasing luminosity.

iii) Model 3: $A/2 = 3 \times 10^{-3}\lambda_{Edd}^{-0.8}$ and $v_b = 580/(M_{BH}/M_\odot)\,s^{-1}$, where $\lambda_{Edd} = \dfrac{\dot{m}}{\dot{m}_{Edd}}$ is the accretion rate. In this model the PSD amplitude depends on the accretion rate and the break frequency is the same as in Model 1.

iv) Model 4: $A/2 = 3 \times 10^{-3}\lambda_{Edd}^{-0.8}$ and $v_b = \dfrac{200}{86400}(L_{44,bol})(M_{6,BH})^{-2}\,s^{-1}$. The PSD amplitude is the same as in Model 3, while the break frequency is the same as in Model 2.

I can now use eq. (25) and compute the model variance for any of the four models, by replacing A and v_b from each model.
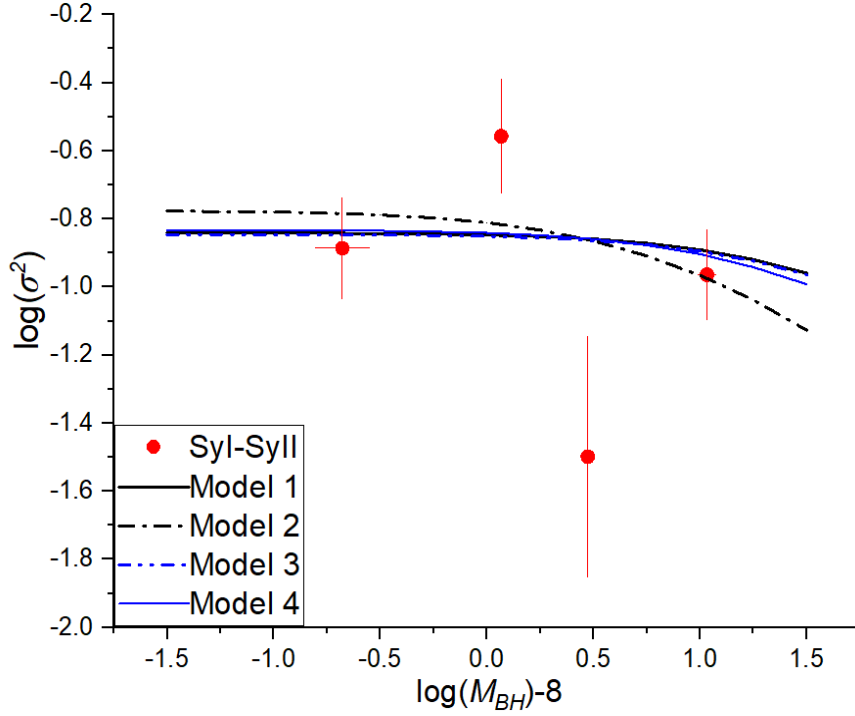
Figure 5.2 *Best fit models to the data shown in Fig. (5.1).*

5.1) Fitting the data

I fitted the data with the models listed above, following the χ^2- minimization method:

i) Fitting Model 1: I considered values of A from 0.005 to 0.094, with a step of ΔA=0.001. For each one of them I calculated σ^2_{mod} for the 4 points shown in Fig. (5.1). The best-fit A value is the one that minimizes the χ^2 statistic, defined as follows:

$$\chi^2 = \sum_{i=1}^{N=4} \left(\frac{\sigma^2_{NXV,i}(M_{BH}) - \sigma^2_{mod,i}(M_{BH})}{\sigma_i} \right)^2 \quad . \qquad (26)$$

ii) Fitting Model 2: For Model 2 I used the same method as above with the addition that for every value of A I also assumed a range of λ_{Edd} , from 0.01 to 0.2, with a step of $\Delta\lambda_{Edd}=$ 0.005, to calculate L_{bol} via the followng relation:

$$\lambda_{Edd} = \frac{L_{bol}}{1.26 \cdot 10^{38} \frac{M_{BH}}{M\odot}} \quad . \qquad (27)$$

For each pair of values (A, λ_{Edd}), I calculated σ^2_{mod} for the 4 points shown in Fig. (5.1), and I chose the ones which provide the smallest χ^2 value, computed as above.

iii) Fitting Model 3&4: For these models I used λ_{Edd} , in order to calculate the both the *PSD* amplitude and ν_b. The rest are the same as in Model 1 and 2.

The best-fit models are plotted in Fig. (5.2), and the best-fit results are listed in table (5.1). The last column lists P_{null}. P_{null} is the probability that we will get the resulting value of χ^2_{min} by chance, if the model is the correct one (null hypothesis). The χ^2_{min} values follow the χ^2 distribution with N-n$_{par}$ degrees of freedom (dof),

where N is the number of data points and n_{par} is the number of fitted parameters. In model 1,3 and 4 there are 3 degrees of freedom (N=4, n_{par}=1), while in model 2 there are 2 degrees of freedom (N=4, n_{par}=2).

	A	σ_A	λ_{Edd}	$\sigma_{\lambda Edd}$	dof	χ^2	P_{null}
Model 1	0.031	±0.006	-	-	3	6.71	0.08
Model 2	0.036	-0.009, +0.01	0.03		2	6.15	0.05
Model 3	0.015(*)		0.13	-0.03, +0.04	3	6.71	0.08
Model 4	0.016(*)		0.13	-0.03, +0.04	3	6.54	0.09

Table 5.1: *Best A and λ_{Edd} results with their errors, min χ^2 and P_{null} for each model. The values with (*) are calculated from the PSD normalization in model 3 and 4.*

The numbers in the 3rd and 5th columns list the 68% confidence interval for the best fit parameters. This interval indicates the parameters for which χ^2 is less than $\chi^2_{min} \pm \Delta \chi^2$. For Model 1,3 and 4, which have 1 free parameter, $\Delta \chi$ =1, while for Model 2, where n_{par}=2, $\Delta \chi$ =2.3.

An example of the method I used to compute the errors is shown in Fig. (5.3). In Model 2, all λ_{Edd} values that I considered are bellow the respective line, $\Delta \chi^2 = 2.3$. In other words, all λ_{Edd} are within the 68% confidence interval of the best fit λ_{Edd} value.
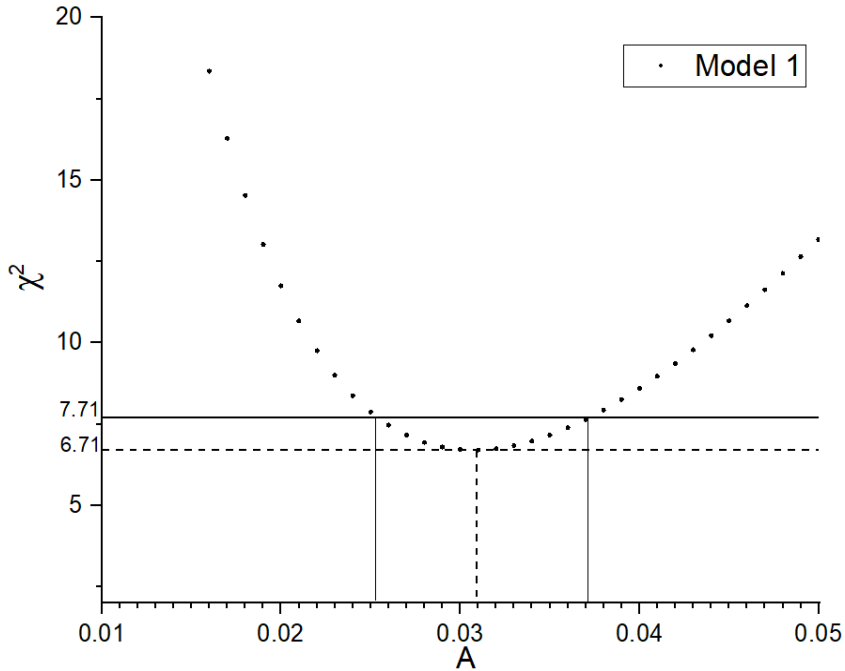
Figure 5.3 *Plot of χ^2 vs A for Model 1. Dashed horizontal line indicates χ^2_{min}=6.71 Black horizontal line indicates the $\chi^2_{min}+\Delta\chi^2$=7.71 value. The two solid, vertical lines indicate the upper and lower limits for the 68% confidence region of A. Dashed vertical line indicated the value A that minimizes the χ^2.*

All models are consistent with the data, since P_{null} >0.01. The *PSD* amplitude, in the case of Model 1, is consistent with the results of Papadakis (2014), who found *A*/2=0.02, within 1.5σ. On the other hand, the best-fit accretion rate of Models 3 and 4 is higher, by a factor of ~2, than the best-fit accretion rate of Paolillo et al. (2017), who studied the excess variance of distant AGN.

CHAPTER 6. CONCLUSIONS

The main object of this project was to compute the normalized excess variance, σ^2_{NXV}, of Seyfert I and II galaxies, and study their dependence on the BH mass. To this end, I collected data from the Burst Alert Telescope (BAT) board on NASA's Neil Gehrels *Swift* satellite. Oh et al. (2018) published the data from the first 105 months of the BAT hard X-ray all-sky survey, including observations carried out between 2004 December and 2013 August (i.e. 8.75 years). There are 1632 sources detected by BAT, during the first 105 months of its operation, and 827 of those are identified as Seyfert galaxies. I selected to study 370 SyI (Seyfert types from 1 up to 1.5) and 448 SyII (Seyfert types from 1.9 to 2) galaxies. For those sources, I retrieved the BAT lightcurves in the $14-195$ keV band.

I ignored the points in the lightcurves with exposure time Δt <40 ksec, to avoid the effects of large experimental errors in the computation of the average Poisson noise. I computed the S/N ratio, for each one of them. Following Paolillo et al. (2017), I chose to keep sources with S/N>0.8, in order to avoid using excess variance measurements with large uncertainty. After that, the number of sources was cut down to 159 and 151 galaxies, in the SyI and SyII samples respectively.

I used the flux (F_{14-195}) and redshift (z) values from the BAT catalog, and I found that the SyI and SyII samples have the same F_{14-195} distribution. Their z distributions are statistically different. The redshift distribution for SyI sources is systematically shifted to higher values, compared with the SyII z distribution. I used the luminosity values, $log(L_{14-195})$, provided by Baumgartner et al. (2013), and I found that the $log(L_{14-195})$ distribution of the SyI and SyII galaxies is significantly different as well. On average, SyI sources are twice as luminous than SyII sources. That may be because all sources have similar fluxes but the SyI sources are more distant than SyII. As a consequence SyI sources are expected to be intrinsically brighter than SyII sources.

I also retrieved the BH mass estimates for 136 sources in the SyI sample and 77 sources in the SyII sample, from Koss et al. (2017). The $log(M_{BH})$ distribution of the SyI and SyII galaxies is significantly different. That may be caused because SyII galaxies need to have large black hole mass in order to be bright enough, so that the *Swift*-BAT can detected them. I used the $log(L_{14-195})$ and $log(M_{BH})$ data to approximate the accretion rate of each source. The sample distribution of the accretion rate for the SyI and SyII sample is significantly different. The accretion rate of the SyI sources is significantly larger than the SyII sources.

To quantify the variability of the sources, I computed the normalized excess variance, σ^2_{NXV}, using the lightcurves from the BAT catalog. Sources with different z have different time duration in their rest frame. So, I converted the time duration in the observer's frame, to time duration in the rest frame of each source, in order to compute σ^2_{NXV} using lightcurves that have the same time duration. Thus, I computed σ^2_{NXV} using a time duration of T=91 months, in the source frame. The sample distribution of the normalized excess variance, σ^2_{NXV}, for the SyI and SyII samples is statistically the same, according to the K-S test results (P_{null} =0.016). However, the SyII distribution is systematically shifted to the right, when compared with the SyI distribution, which implies that the X-ray variability amplitude may be larger in the SyII galaxies.

I examined the correlation between σ^2_{NXV} and $log(L_{14-195})$ in the SyI and SyII sample. I fitted the data with a straight line (in the log-log space), using the method of least squares. Qualitatively, the dependence of σ^2_{NXV} on $log(L_{14-195})$ is the same for both SyI and SyII: σ^2_{NXV} appears to decrease with increasing $log(L_{14-195})$. The best-fit slopes are consistent within the errors, but the normalization of the SyII best-fit lines is significantly larger than the respective normalization for the SyIs, indicating larger variability amplitude for SyIIs. Actually, this is in agreement with the differences between σ^2_{NXV} distribution, for the two samples.

I also examined the correlation between σ^2_{NXV} and $log(M_{BH})$. The SyII sources are shifted to higher values of σ^2_{NXV} than the SyI source, as expected. I fitted the data for the SyI sources with a linear model, as above.

In order to test if the SyII data are consistent with the best fit to the SyI data, I calculated the distance of the SyII data from the SyI best-fit for line, and I found it was consistent with zero. So, formally, the normalized excess variance, for both SyI and SyII, have the same dependence on $log(M_{BH})$. Finally, I considered the σ^2_{NXV} vs $log(M_{BH})$ relation for a sub-sample of SyI and SyII galaxies with similar accretion rate distribution. In this case, I considered recently developed models, which predict the observed σ^2_{NXV} based on the power-spectrum results from the analysis of nearby Seyferts. In particular, I considered the four models introduced by Paolillo et al. (2017), which are based on the hypothesis of a bending power-law model for the PSD, and assuming various dependence of the break frequency, ν_b, and the PSD amplitude, A, on the BH mass and the accretion rare, λ_{Edd} .

 All four models are consistent with the σ^2_{NXV} vs $log(M_{BH})$ plot of the sources with similar accretion rate. The best-fit PSD amplitude is in agreement with the previous estimation of Papadakis (2014), based in excess variance measurements of local AGN. On the other hand, the best-fit λ_{Edd} is higher, by a factor of ~2, than the one estimated by Paolillo et al. (2017), for distant AGN. In general, I found that the variability amplitude of AGN in the local Universe is similar to what has been observed in the past for nearby AGN, and with the variability properties of distant AGN.

REFERENCES

Allevato V.; Paolillo M.; Papadakis I.; Pinto C., 2013, ApJ 771 9

Barthelmy S. D.; Barbier L. M.; Cummings J. R.; Fenimore E. E.; Gehrels N.; Hullinger D.; Krimm H. A.; Markwardt C. B.; Palmer D. M.; Parsons A.; Sato G.; Suzuki M.; Takahashi T.; Tashiro M.; Tueller J., 2005

Baumgartner W. H.; Tueller J.; Markwardt C. B.; Skinner G. K.; Barthelmy S.; Mushotzky R. F.; Evans P.; Gehrels N., 2013, ApJS, 207, 19

Bentz M. C.; Katz S., 2015, PASP, 127, 947, (http://www.astro.gsu.edu/AGNmass/)

González-Martín O.; Vaughan S., 2012, A&A, 544, A80

Greene J. E.; Ho L. C., 2005a, ApJ, 627, 721

Kormendy J.; Ho L. C., 2013, ARA&A, 51, 511

Koss M.; Trakhtenbrot B.; Ricci C.; Lamperti I.; Oh K.; Berney S.; Schawinski K.; Baloković M.; Baronchelli L.; Crenshaw D. M.; Fischer T.; Gehrels N.; Harrison F.; Hashimoto Y.; Hogg D.; Ichikawa K.; Masetti N.; Mushotzky R.; Sartori L.; Stern D.; Treister E.; Ueda Y.; Veilleux S.; Winter L., 2017 ApJ, 850, 74

Nandra K.; George I. M.; Mushotzsky R. F., et al. 1997, ApJ, 476, 70

Oh K; Koss M.; Markwardt C. B.; Schawinski K.; Baumgartner W. H.; Barthelmy S. D.; Cenko S. B.; Gehrels N.; Mushotzky R.; Petulante A; Ricci C.; Lien A.; Trakhtenbrot B.,2018, ApJS, 235, 4 (https://swift.gsfc.nasa.gov/results/bs105mon/)

Papadakis I. E., 2004, MNRAS, 348, 207

Paolillo M.; Papadakis I.; Brandt W. N.; Luo B.; Xue Y. Q.; Tozzi P.; Shemmer O.; Allevato V.; Bauer F. E.; Comastri A.; Gilli R.; Koekemoer A. M.; Liu T.; Vignali C.; Vito F.; Yang G.; Wang J. X.; Zheng X. C., 2017, MNRAS, 471, 4398-4411

Ricci C; Trakhtenbrot B.; Koss M. J.; Ueda Y.; Del Vecchio I.; Treister E.; Schawinski K.; Paltani S., Oh K.; Lamperti I.; Berney S.; Gandhi P.; Ichikawa K.; Bauer F. E.; Ho L. C.; Asmus D.; Beckmann V.; Soldi S.; Baloković M.; Gehrels N.; Markwardt C. B., 2017, ApJS, 233, 17

Trakhtenbrot B.; Netzer H., 2012, MNRAS, 427, 3081

https://en.wikipedia.org/wiki/Neil_Gehrels_Swift_Observatory

http://ned.ipac.caltech.edu/

BIBLIOGRAPHY

Bradley M. Peterson, An Introduction to Active Galactic Nuclei, Cambridge University Press; 1997

Bradley W. Carroll, Dale A. Ostlie, An Introduction to Modern Astrophysics, Second Edition, Cambridge University Press; 201

APPENDIX

#	Type	z	S/N	σ^2_{NXV}	$F_{14\text{-}195}$ (A*)	$\log L_{14\text{-}195}$ (B*)	$\log L_{bol}$ (B)	$\log M_{BH}$
								1	2	3	4	5
6	1.2	0.0258	0.88	0.017	15.97	43.4	44.36	-	-	7.29	6.86	7.23
10	2	0.0956	1.15	0.126	19.6	44.55	45.5	9.16	-	-	-	-
13	2	0.012	0.84	0.141	19.57	43.06	43.71	-	-	-	-	-
16	1.2	0.142	0.82	-0.362	14.01	44.84	45.72	-	-	7.93	-	8.49
18	1.9	0.105	0.93	-0.047	15.84	44.56	45.49	-	-	-	8.84	-
20	2	0.074	0.83	0.54	19.47	45.3	46.24	-	-	-	-	-
22	1.2	0.0476	0.88	0.001	16.34	43.9	-	-	-	-	-	-
30	1	0.1408	0.93	0.284	26.08	44.56	-	-	-	-	-	-
36	1.5	0.064	1.67	-0.069	28.06	44.45	45.31	-	-	7.82	-	-
43	1.2	0.0149	1.59	0.137	31.13	43.13	44.09	-	-	7.21	6.9	-
53	2	0.041	0.9	-0.101	17.93	43.83	44.69	-	-	-	-	-
55	2	0.0475	1.03	2.196	15.27	43.8	44.65	8.08	-	-	-	-
57	2	0.0597	1.4	0.159	27.68	44.48	-	-	-	-	-	-
61	1.2	0.0527	1.36	-0.051	24.04	44.23	45.16	-	-	7.74	7.96	-
72	2	0.0191	4.49	0.128	73.91	43.69	44.61	8.17	-	-	-	-
73	1.2	0.047	2.93	-0.001	48.39	44.42	45.29	-	-	8.05	7.91	8.3
74	2	0.0195	1.05	0.254	24.47	43.22	44.13	7.89	-	-	-	-
77	1.5	0.0174	0.95	0.011	13.57	42.94	43.83	7.03	-	6.61	6.14	-
78	1	0.046	1.08	-0.016	20	43.97	-	-	-	-	-	-
83	2	0.0165	0.83	-0.116	14.48	42.98	43.84	7.69	-	-	-	-
84	2	0.0298	2.14	0.128	48.97	44.33	44.95	8.99	-	-	-	-
85	1.9	0.079	0.96	-0.228	19.27	44.54	45.45	-	-	-	-	-
87	2	0.0252	3.51	0.051	67.37	44.15	44.9	8.45	-	-	-	-
96	2	0.0172	1.11	-0.021	24.02	43.2	44.09	-	-	-	-	-
98	1	0.082	0.95	-0.198	13.24	44.25	-	-	-	-	-	-
102	2	0.0136	3.83	0.068	77.51	43.66	44.43	8.21	-	-	-	-
106	1.2	0.0424	1.16	0.108	24.27	44.11	45.06	-	-	8.03	7.48	-
107	1	0.1096	0.93	-0.122	20.23	44.72	-	-	-	-	-	-
113	1	0.0492	3.59	0.031	55.63	44.46	45.37	-	-	8.08	-	-
119	2	0.0288	0.89	0.34	16.83	46.06	44.46	-	-	-	-	-
129	1.5	0.0167	3.42	0.046	62.22	43.58	44.46	-	-	7.29	7.05	-
133	2	0.0162	2.48	0.45	48.41	43.26	44.16	8.86	-	-	-	-
134	1.5	0.043	1.5	0.024	30.21	44.12	45.04	-	-	7.92	7.99	-
135	1.9	0.0592	0.98	-0.411	21.21	44.22	45.2	-	-	-	-	-
138	1.9	0.0618	0.87	0.097	15.13	44.09	44.98	-	-	-	-	-
147	1.2	0.044	5.15	0.026	92.09	44.71	45.62	-	-	8.09	-	-
149	2	0.0579	1.16	-0.06	29.01	44.5	45.34	9.15	-	-	-	-
151	2	0.0152	1.15	0.039	24.59	43.42	44.06	-	-	-	-	-
156	2	0.0168	1.31	-0.011	25	43.24	44.12	7.79	-	-	-	-
157	2	0.0289	3.08	0.217	74.31	44.37	45.13	9.25	-	-	-	-
159	2	0.0163	1.39	0.276	31.13	43.25	44.2	-	-	-	-	-
162	1.5	0.0326	1.54	0.24	27.51	43.63	44.54	-	-	8.71	-	-
163	2	0.0136	1.61	-0.004	36.22	43.68	44.08	8.12	7.83	-	-	-
167	1.2	0.067	1.28	-0.039	23.06	44.37	45.31	-	-	8	-	-
171	2	0.0238	0.88	0.382	15.47	43.23	44.13	7.82	-	-	-	-
172	2	0.0901	0.84	0.115	18.82	44.51	45.45	-	-	-	-	-
176	2	0.0477	0.81	0.068	18.68	43.97	-	-	-	-	-	-
183	1.5	0.0558	1.2	0.013	24.8	44.24	45.14	-	-	8.05	7.68	-
184	2	0.0055	3.94	0.086	63.52	42.6	43.31	-	-	-	-	-
193	2	0.0365	0.93	0.052	21.67	44.34	44.71	-	-	-	-	-
200	2	0.0747	0.89	-0.087	19.37	44.32	45.33	-	-	-	-	-
207	1.9	0.0552	0.82	0.523	12.12	43.87	44.8	-	-	-	-	-
209	2	0.089	1.06	0.398	22.01	44.83	45.64	-	-	-	-	-
213	1.5	0.0379	1.39	-0.092	19.28	43.8	44.8	-	-	7.85	-	-
214	1.2	0.0485	5.87	0.022	118.67	44.81	45.73	-	-	8.27	-	-
216	1.5	0.005	0.99	0.568	19.54	42.05	42.49	7.74	-	-	5.74	-
217	2	0.0435	0.99	0.096	22.16	43.95	44.88	-	-	-	-	-

218	2	0.045	1.14	0.045	24.23	44.22	44.98	-	-	-	-	-
220	1.5	0.104	1.76	-0.01	25.26	44.83	45.74	-	-	8.07	8.08	-
228	1.2	0.0355	0.83	0.125	18.3	43.69	44.6	-	-	7.5	7.35	-
230	1.2	0.0364	1.07	-0.119	18.08	43.74	44.66	-	-	8.33	7.72	-
231	2	0.0577	0.81	-0.204	14.73	43.95	-	-	-	-	-	-
236	1	0.0217	1.69	0.108	33.75	43.58	-	-	-	-	-	-
237	2	0.0113	2.31	0.497	49.38	43.12	44.01	8.17	-	-	-	-
238	2	0.147	0.87	0	17.03	44.97	-	-	-	-	-	-
242	1.5	0.0159	1.51	0.245	34.23	43.23	44.13	-	-	7.25	7.23	-
243	1.9	0.0907	1.11	0.05	20.08	44.61	45.54	-	-	-	7.92	-
244	1.5	0.029	2.73	0.172	54.1	44.05	44.98	-	-	8.12	7.54	-
245	2	0.0294	1.47	-0.019	26.34	43.99	44.66	8.31	-	-	-	-
247	2	0.0181	1.36	0.023	24.49	43.23	44.1	-	-	-	-	-
254	1.5	0.0577	1.01	0.043	20.22	44.21	45.11	-	-	7.97	8.4	-
258	2	0.035	3.02	0.068	58.27	44.21	45.17	-	-	-	-	-
261	1.5	0.0179	5.19	0.195	119.8	43.82	44.69	-	-	7.29	7.06	6.88
266	1	0.0323	3.48	0.017	74.29	44.21	45.13	-	-	8.72	8.27	8.07
267	2	0.0212	1.07	-0.144	23.11	43.29	-	-	-	-	-	-
269	1.5	0.0125	2.84	0.087	48.89	43.23	44.14	-	-	7.42	6.88	-
270	2	0.0351	2.27	0.114	37.32	44.03	44.94	-	-	-	-	-
274	1.5	0.049	0.99	-0.065	19.15	44	44.92	-	-	8.76	8.43	-
279	2	0.0278	0.89	0.42	15.83	43.4	44.29	8.05	-	-	-	-
301	1	0.0099	1.14	-0.045	22.68	42.65	43.48	-	-	6.98	-	-
303	2	0.066	1.13	-0.121	25.35	44.42	45.36	-	-	-	-	-
304	2	0.036	1.06	0.399	22.01	43.88	44.76	-	-	-	-	-
308	2	0.0078	14.82	0.209	328.93	43.63	44.59	9.25	-	-	-	-
309	1	0.0585	1.06	0.282	13.36	44.06	-	-	-	-	-	-
310	1.5	0.0205	7.11	0.193	141.21	44.1	44.99	-	-	7.62	7.83	-
313	1.2	0.0339	2.02	0.04	27.45	43.88	44.81	-	-	6.87	7.06	-
314	1	0.1372	1.28	0.071	18.18	44.97	45.94	-	-	7.33	-	-
316	1.2	0.033	3.19	0.056	62.28	44.19	45.11	-	-	7.79	8.09	-
317	2	0.0154	1.08	0.084	23.06	43.11	44.01	8.94	-	-	-	-
318	1.5	0.0892	0.86	-0.007	10.39	44.35	45.28	-	-	8.12	8.19	-
319	2	0.0062	1.44	0.101	30.89	42.73	43.21	-	-	-	-	-
329	2	0.0403	1.77	-0.022	29.69	44.08	44.94	-	-	-	-	-
330	2	0.0224	1.24	0.128	24.12	43.69	44.35	-	-	-	-	-
342	1.2	0.0248	2.03	0.017	39.49	43.71	44.63	-	-	-	-	-
344	2	0.061	0.89	0.123	22.19	44.19	45.12	-	-	-	-	-
345	2	0.047	1.26	-0.075	31.87	44.25	45.19	8.12	-	-	-	-
347	1.5	0.0188	3.06	0.049	56.7	43.66	44.6	-	-	8.2	7.97	8.1
360	2	0.1108	0.91	0.044	21.34	44.78	45.7	-	-	-	-	-
366	1.5	0.0614	1.37	0.218	22.53	44.35	-	-	-	-	-	-
370	2	0.0294	0.83	0.003	18.94	43.62	-	-	-	-	-	-
372	1.9	0.123	0.96	0.558	19.05	44.87	45.8	-	-	-	9.31	-
379	2	0.0258	1.26	0.028	27.78	43.57	44.53	-	-	-	-	-
382	1.5	0.0222	2.53	-0.006	42.72	43.7	44.62	-	-	7.64	7.52	7.61
384	1.2	0.023	1.24	-0.054	19.54	43.4	44.33	-	-	7	6.82	-
385	2	0.0159	0.87	0.249	22.41	43.08	43.9	7.81	-	-	-	-
398	1.2	0.04	2.92	0.038	51.15	44.25	45.18	-	-	8.45	8.09	-
402	1.5	0.0405	1.26	0.102	20.12	43.9	-	-	-	-	-	-
403	1.5	0.0468	0.88	0.244	19.81	43.94	44.86	-	-	7.69	7.67	-
409	1	0.1	1.02	0.123	16.72	44.58	45.46	-	-	8.13	-	8.73
411	1.2	0.0331	1.04	0.152	22.17	43.74	44.66	-	-	6.99	7.2	-
413	2	0.089	0.98	0.033	22.24	44.58	45.53	-	-	-	-	-
416	2	0.0218	1.86	0.154	39.15	43.76	44.62	8.14	-	-	-	-
418	1.5	0.1263	0.93	0.277	14.91	44.71	45.64	-	-	8.56	8.33	-
420	1.2	0.0919	0.91	0.122	15.3	44.53	45.45	-	-	9.13	8.77	-
423	1.5	0.0316	1.68	0.049	31.7	43.81	-	-	-	-	-	-
426	2	0.0647	0.88	0.099	18.91	44.38	45.11	8.77	-	-	-	-
429	1.5	0.1338	0.88	0.268	15.31	44.85	45.77	-	-	-	8.78	-
431	1	0.137	0.85	-0.169	12.68	44.79	45.71	-	-	8.98	-	-
432	1.9	0.0606	1.07	-0.003	21.5	44.19	45.15	-	-	-	7.69	-

434	2	0.036	0.91	0.053	15.98	43.76	44.63	8.35	-	-	-	-
440	2	0.0133	1.13	-0.014	21.46	43.7	43.82	8.71	-	-	-	-
441	1	0.0391	1.37	0.062	28.82	44	-	-	-	-	-	-
446	2	0.0268	0.98	-0.104	18.59	43.52	44.32	7.61	-	-	-	-
447	1	0.0573	1.83	-0.017	29.09	44.39	45.3	-	-	8.58	8.38	-
449	1.2	0.0292	2.1	0.007	36.84	43.81	44.72	-	-	8.48	8.03	-
451	2	0.0075	1.07	0.115	19.11	42.39	43.75	7.1	-	-	-	-
453	2	0.0196	2.34	0.045	46.38	43.55	44.45	7.88	-	-	-	-
455	1.2	0.0323	2.08	0.015	35.66	43.97	44.91	-	-	7.34	7.04	-
456	2	0.0422	1.04	0.082	14.1	44.1	44.81	-	-	-	-	-
458	1.5	0.0353	3.45	0.049	60.95	44.21	45.13	-	-	6.64	6.93	7.29
460	1.2	0.0291	1.16	-0.175	18.03	43.48	44.39	-	-	7.04	6.92	-
466	1.2	0.1222	0.85	0.081	10.69	44.69	45.62	-	-	7.94	8.01	-
470	1.5	0.0214	0.83	-0.257	13.55	43.08	44.07	-	-	7.03	6.72	-
473	1.2	0.0858	1.33	-0.012	22.82	44.63	45.55	-	-	8.61	8.22	-
474	2	0.0581	0.82	-0.213	14.79	44.22	45	9.15	-	-	-	-
480	2	0.008	3.6	0.04	81.89	43.29	43.75	8.41	-	-	-	-
482	1	0.037	1.02	-0.137	15.69	43.74	-	-	-	-	-	-
484	2	0.0037	1.97	0.108	36.74	42.53	43.06	8.27	6.38	-	-	-
488	2	0.0573	0.95	-0.071	18.02	43.97	44.92	-	-	-	-	-
489	2	0.0333	1.34	-0.041	29.66	44	44.86	-	-	-	-	-
492	2	0.0284	0.82	0.437	23.5	43.61	44.47	-	-	-	-	-
497	1.5	0.0039	6.9	0.081	112.47	42.55	43.57	-	7.18	6.78	6.62	6.77
501	1	0.086	1.78	-0.04	31.47	44.77	45.67	-	-	8.59	8.35	-
502	2	0.0107	4.06	0.037	81.21	43.48	44.28	-	-	-	-	-
507	1.5	0.06	1.33	0.041	24.88	44.25	45.26	-	-	8.36	-	-
509	2	0.02	1.1	0.214	20.92	43.31	44.41	8.52	-	-	-	-
512	1.5	0.0476	0.86	0.081	12.77	43.83	44.79	-	-	7.91	7.8	-
513	2	0.0336	0.83	-0.211	14.8	43.58	44.39	-	-	-	-	-
517	2	0.0205	1.21	0.118	21.35	43.29	44.17	8.15	-	-	-	-
518	2	0.0125	0.99	-0.15	27.35	43.08	43.89	-	7.52	-	-	-
519	2	0.0328	1.94	0.048	33.05	44.09	44.8	8.15	-	-	-	-
520	2	0.0175	1.01	-0.074	18.38	43.13	44.09	8.12	-	-	-	-
530	1.2	0.0088	6.79	0.132	112.42	43.29	44.49	-	-	7.62	7.43	7.39
538	1.9	0.056	0.87	0.026	14.98	44.09	44.97	-	-	-	-	-
542	1.2	0.0211	1.3	0.088	20.13	43.28	44.19	8.02	-	7.05	6.82	6.67
544	1.9	0.1055	1.06	0.075	20.85	44.62	45.55	-	-	-	-	-
549	1.2	0.0437	1.04	-0.018	17.59	43.82	44.75	8.63	-	7.97	7.29	-
552	1	0.0299	0.98	-0.147	12.91	43.43	44.33	-	-	7.14	7.4	-
556	1.5	0.0601	1.58	-0.004	23.26	44.24	45.18	-	-	7.98	7.75	-
558	1.2	0.0097	8.3	0.068	173.84	43.58	44.6	-	-	7.29	7.27	7.37
561	1.5	0.0632	1.03	-0.294	21.71	44.17	45.16	-	-	7.76	7.42	-
562	2	0.0209	0.91	-0.023	18.11	43.13	-	-	-	-	-	-
566	1.2	0.0065	1.78	0.029	26.85	42.38	43.28	-	-	5.66	5.32	-
567	1.2	0.0329	2.6	0.043	48.28	44.11	45.02	-	-	7.31	7.07	-
568	2	0.0099	0.9	0.145	14.69	42.52	43.45	8.61	-	-	-	-
576	1.2	0.049	0.82	-0.111	16.89	43.92	44.86	-	-	7.47	-	-
582	2	0.036	0.95	0.284	21.56	43.79	44.7	8.31	-	-	-	-
584	2	0.028	2.68	0.033	49.46	43.91	44.83	7.98	-	-	-	-
585	1.5	0.0023	3.23	0.025	42.49	41.65	42.92	-	-	5.34	5.6	3.13
586	2	0.0224	1.5	0.189	29.18	43.56	44.44	8.18	-	-	-	-
590	2	0.0028	1.72	0.05	32.05	42.09	43.05	8.75	-	-	-	-
592	2	0.0242	1.42	0.018	23.91	43.48	44.39	7.82	-	-	-	-
593	2	0.003	1.39	0.54	24.35	41.79	43.09	7.3	-	-	-	-
595	1.5	0.0033	38.64	0.094	618.88	43.1	43.92	-	7.58	7.12	-	7.56
596	1.2	0.0228	1.38	0.07	20.09	43.37	44.31	-	-	7.39	7.02	-
605	2	0.0632	1.13	-0.103	18.77	44.2	45.08	8.33	-	-	-	-
607	1.2	0.008	2.19	0.339	38.62	42.64	43.29	8	-	7.68	7.14	-
608	1.5	0.0129	1.97	0.075	26.17	42.9	43.8	-	-	6.17	6.32	6.82
611	1	0.0708	1.22	-0.186	17.17	44.33	45.18	-	-	8.61	4.5	-
613	1	0.0234	1.32	0.042	21.6	43.45	44.38	-	-	7.57	7.25	7.42
615	2	0.0084	13.84	0.142	278.91	43.7	44.07	6.99	6.94	-	-	-

616	2	0.0011	1.93	0.088	27.53	40.82	41.69	-	-	-	-	5.45
629	2	0.025	3.97	0.362	90.68	44.26	45	8.99	-	-	-	-
630	2	0.0367	1.14	0.193	35.33	44.07	44.99	8.16	-	-	-	-
631	1	0.009	4.11	0.038	88.3	43.2	43.96	-	-	7.27	6.9	6.88
634	1.9	0.055	0.89	0.094	21.11	44.07	44.95	-	-	-	7.71	-
636	1.5	0.0244	2.2	0.21	44.9	43.79	44.72	-	-	8.25	7.68	-
638	2	0.0167	1.74	0.092	25.52	43.35	44.14	9.8	-	-	-	-
651	1.5	0.0672	1.15	0.14	16.79	44.25	45.18	-	-	7.44	7.65	-
1415	1.2	0.0467	0.84	0.123	16.81	43.98	-	-	-	-	-	-
652	1.5	0.0299	1.89	0.122	30.86	43.8	44.74	-	-	7.73	7.65	-
653	2	0.0037	0.9	0.046	20.16	41.89	42.84	7.03	-	-	-	-
654	2	0.0104	1.3	0.215	26.54	42.82	43.69	7.52	-	-	-	-
655	2	0.0019	10.72	0.106	282.11	43.13	-	-	-	-	-	-
657	1.5	0.015	2.26	0.014	30.85	43.24	44.16	-	-	6.98	7	-
659	2	0.0251	2.65	0.058	54.42	43.97	44.79	8.54	-	-	-	-
660	1	0.104	0.95	-0.007	24.71	44.95	45.86	-	-	-	-	-
663	1.5	0.034	0.84	0.664	12.48	43.6	44.4	-	-	7.37	-	-
666	2	0.0366	1.31	-0.186	16.21	43.73	44.6	8.67	-	-	-	-
667	1.5	0.0705	1.06	-0.069	17.94	44.26	45.2	-	-	8.84	-	-
669	2	0.0319	0.85	0.02	18.29	43.58	44.44	8.51	-	-	-	-
677	2	0.013	1.2	0.22	18.21	42.95	43.74	-	-	-	-	-
682	2	0.023	5.28	0.27	103.15	44.1	45.04	8.87	9	-	-	-
683	1.2	0.0418	0.98	0.278	25.17	43.98	44.86	-	-	7.28	-	-
686	1.5	0.0035	0.84	0.185	15.95	41.48	42.53	7.11	-	6.71	6.14	6.66
688	2	0.0086	1.07	0.325	14.87	42.46	43.35	7.76	-	-	-	-
694	1.5	0.016	12.97	0.058	263.25	44.21	45.12	-	-	7.84	-	-
697	1.5	0.0304	2.27	0.239	34.66	43.91	44.81	-	-	8	7.55	7.43
699	2	0.052	1.02	-0.097	22.1	44.15	45.04	-	-	-	-	-
702	1.5	0.0501	1.15	-0.01	18.19	44.08	45.02	-	-	7.93	7.88	-
711	2	0.0014	15.09	0.031	273.17	42.43	-	-	-	-	-	-
713	1.5	0.0986	1.01	0.067	15.14	44.63	45.56	-	-	8.87	-	-
714	2	0.076	0.88	0.151	23.77	44.86	45.41	8.8	-	-	-	-
717	1.5	0.0172	4.99	0.067	86.47	43.7	44.61	-	-	8.03	7.77	7.72
719	1	0.0224	1.79	0.128	39.27	43.66	44.58	-	-	7.13	6.94	-
722	1.2	0.0723	1.33	0.019	17.42	44.37	45.28	-	-	8.35	8.12	-
723	2	0.0169	1.12	0.025	17.04	43.09	44	7.81	-	-	-	-
728	1	0.0865	1.1	-0.037	17.87	44.5	45.42	-	-	8.67	8.38	9.01
733	2	0.0249	0.92	0.4	21.07	43.37	44.26	7.65	-	-	-	-
735	1.2	0.0314	1.83	-0.034	28.77	43.77	44.66	-	-	8.1	7.97	7.59
736	1.5	0.1445	0.81	-0.167	22.18	44.99	45.93	-	-	-	-	-
748	1	0.049	1.23	-0.904	22.8	44.09	45.03	-	-	8.38	8.23	-
750	1.5	0.016	1.11	0.108	19.9	43.08	44.01	-	-	6.86	6.76	-
751	2	0.0163	1.48	-0.039	25.96	43.28	44.1	-	-	-	-	-
753	1.2	0.0364	1.72	0.007	33.3	44.07	44.95	-	-	7.81	7.61	-
760	1.5	0.0446	1.24	0.209	32.67	44.14	45.07	-	-	7.24	6.81	-
765	1.2	0.0684	1.53	0.142	29.35	44.5	45.44	-	-	8.96	8.25	-
766	2	0.0086	1.18	0.295	20.44	42.54	43.45	8.66	-	-	-	-
774	1.5	0.0296	1.7	-0.047	23.79	43.64	44.61	-	-	7.64	7.54	7.28
778	2	0.038	0.91	0.002	14.24	43.72	44.57	9.18	-	-	-	-
795	1.5	0.0156	1.4	0.108	31.91	43.26	44.15	-	-	7.26	6.63	-
797	1	0.129	0.83	-0.087	9.54	44.73	45.64	-	-	8.99	8.86	8.34
804	2	0.0274	1.13	0.138	19.79	43.6	44.35	9.82	-	-	-	-
811	2	0.0547	2.75	0.04	42.97	44.51	45.42	-	-	-	-	-
823	2	0.009	1	-0.029	23.57	42.76	43.51	-	-	-	-	-
1485	1	0.0264	0.89	-0.449	20.34	43.54	-	-	-	-	-	-
833	1	0.031	1.56	0.444	32.71	43.99	44.91	-	-	-	-	-
837	2	0.0091	1.43	0.21	19.46	44.31	-	-	-	-	-	-
838	2	0.005	1.57	-0.002	22.41	42.06	-	-	-	-	-	-
839	2	0.0291	0.91	0.045	13.81	43.47	-	-	-	-	-	-
846	1.2	0.054	2.11	0.001	43.23	44.49	45.4	-	-	8.25	7.77	-
875	2	0.0037	5.17	0.026	96.37	42.51	43.3	-	-	-	-	-
883	1.5	0.04	1.08	-0.156	22.63	43.8	44.78	-	-	6.98	6.9	-

896	1	0.0214	5.88	0.015	119.04	44.09	-	-	-	-	-	-
898	2	0.017	1.04	0.046	17.63	43.15	-	-	-	-	-	-
905	1	0.037	1.69	0.052	41.54	44.17	45.05	-	-	7.79	7.53	-
912	1.5	0.1106	1.18	-0.097	19.9	44.81	45.73	-	-	8.82	8.49	-
942	2	0.0265	1.08	0.059	20.96	43.65	-	-	-	-	-	-
948	1.2	0.036	1.98	-0.021	42.36	44.05	44.97	-	-	7.76	7.6	-
960	2	0.0412	1.1	0.203	22.11	43.83	44.78	8.11	-	-	-	-
970	2	0.0169	1.83	0.04	39.08	43.46	44.33	-	-	-	-	-
976	1	0.037	0.99	-0.051	19.26	43.81	-	-	-	-	-	-
978	2	0.022	1.08	0.192	16.72	43.32	44.2	7.72	-	-	-	-
984	1.2	0.0579	4.67	0.031	82.33	44.78	45.74	-	-	8.19	8.45	-
994	1.5	0.0561	6.39	0.03	102.87	44.87	45.78	-	-	8.11	9.42	8.64
995	1.5	0.0142	2.07	0.023	36.51	43.25	44.15	-	-	7.1	6.6	-
1002	1.9	0.0741	0.86	0.028	11.16	44.34	45.25	-	-	-	-	-
1013	1.2	0.084	1.68	0.082	33.45	44.72	45.62	-	-	8.29	7.83	-
1015	1.9	0.0563	0.81	0.122	16.87	44.08	44.98	-	-	-	-	-
1016	1	0.042	1.42	0.071	23.58	43.98	-	-	-	-	-	-
1020	2	0.0151	1.12	-0.062	20.35	42.99	43.91	-	-	-	-	-
1032	1.2	0.036	3.03	0.001	58.77	44.21	45.14	-	-	8.07	7.92	-
1040	1.5	0.0629	1.35	-0.008	26.19	44.47	45.33	-	-	8.15	8.04	-
1041	1.2	0.0578	1.22	-0.02	21.85	44.23	45.13	-	-	7.88	8.04	-
1042	1.5	0.0103	1.41	-0.168	25.15	42.76	43.65	-	-	6.56	6.22	-
1043	1.2	0.04	0.95	-0.269	17.49	43.74	44.65	-	-	7.23	6.22	-
1045	1.2	0.052	1.11	0.222	24.92	44.13	45.05	-	-	8.1	7.86	-
1046	1.5	0.0052	3.01	0.109	64.47	42.75	43.59	-	-	6.87	6.46	7.04
1049	2	0.0539	1.4	0.018	23.51	44.22	45.1	9.01	-	-	-	-
1051	2	0.059	1.1	0.033	29.65	44.57	45.35	9.15	-	-	-	-
1057	2	0.0561	7.68	0.085	145.23	45	45.91	-	9.43	-	-	-
1063	1.2	0.0249	1.12	-0.12	19.69	43.4	44.32	-	-	6.48	6.45	-
1072	2	0.06	1.22	-0.033	28.74	44.49	45.36	-	-	-	-	-
1073	2	0.0144	1.51	-0.043	26.22	43.11	-	-	-	-	-	-
1074	2	0.017	0.82	0.036	14.8	42.95	43.88	-	-	-	-	-
1077	2	0.0139	3.26	0.057	75.09	43.12	44.43	-	-	-	-	-
1088	1	0.104	3.41	0.028	51.18	45.15	46.06	-	-	9.6	9.45	-
1089	1.2	0.05	0.94	0.13	16.63	44.03	44.92	-	-	8.39	7.88	-
1090	1.2	0.0344	5.02	0.145	100.14	44.41	45.32	-	-	8.07	8.13	8.05
1092	2	0.0114	3.08	0.026	67.76	43.41	44.23	-	-	-	-	-
1099	1.2	0.0265	0.99	0.106	18.78	43.5	44.41	-	-	7.5	7.03	-
1102	1.2	0.084	2.01	0.069	33.75	44.78	45.69	-	-	8.9	8.7	-
1106	1.5	0.0507	0.84	0.018	13.56	43.87	44.81	-	-	8.37	7.57	-
1110	1.2	0.02	11.78	0.078	210.38	44.05	44.91	-	-	7.63	6.04	-
1111	1	0.0147	3	0.044	39.43	43.25	-	-	-	-	-	-
1117	1.5	0.025	1.38	-0.022	22.65	43.49	44.41	-	-	7.11	6.82	-
1118	1.2	0.0588	1.56	-0.098	33.58	44.38	45.29	-	-	8.01	6.82	-
1121	1.5	0.0248	0.94	0.022	17.28	43.36	-	-	-	-	-	-
1122	1.2	0.114	0.83	0.318	9.26	44.56	45.45	-	-	7.8	8.2	-
1133	2	0.0266	1.71	0.144	31.96	43.68	44.63	-	-	-	-	-
1135	2	0.0087	7.17	0.125	160.02	43.32	44.27	8.45	-	-	-	-
1138	2	0.0611	0.99	0.31	16.16	44.2	-	-	-	-	-	-
1151	1.5	0.0562	2.13	0.021	39.82	44.67	45.47	-	-	7.99	8.1	-
1153	1.2	0.113	0.92	0.117	16.71	44.82	45.76	-	-	8.08	8.09	-
1158	2	0.0225	1.54	-0.007	36.45	43.76	44.54	-	-	-	-	-
1162	1.5	0.025	0.97	-0.112	18.56	43.37	44.28	-	-	7.61	7.1	-
1165	1.9	0.0811	1.52	0.076	30.48	44.76	45.63	8.99	-	-	5.94	-
1172	1.2	0.064	5.48	0.021	99.53	44.98	45.91	-	-	8.44	8.03	-
1174	2	0.0283	0.88	-0.031	13.03	43.51	-	-	-	-	-	-
1177	2	0.017	0.83	0.025	21.45	43.23	44.01	9.8	-	-	-	-
1178	1.5	0.0345	1.25	0.082	24.58	43.83	44.71	-	-	6.92	7.01	-
1179	2	0.149	0.8	0.02	12.24	44.59	45.56	-	-	-	-	-
1180	2	0.0066	1.02	0.586	18.98	42.11	-	-	-	-	-	-
1182	1.5	0.0163	3.8	0.024	70.63	43.59	44.49	-	-	7.32	7.11	6.96
1183	1.5	0.0469	5.77	0.079	110.22	44.75	45.67	-	-	8.55	8.4	-

1188	2	0.0052	4.22	0.05	82.28	43.29	43.53	-	7.74	-	-	-
1189	1	0.0295	2.67	0.006	52.96	44	44.9	-	-	8.61	8.48	-
1195	1.2	0.12	0.87	0.2	19.27	44.82	45.71	-	-	8.43	8.17	-
1202	2	0.0174	1.05	0.133	20.9	43.31	44.03	8.69	-	-	-	-
1210	2	0.0963	0.87	0.281	17.43	44.5	-	-	-	-	-	-

Table A.1: *Table with the number in 105-BAT catalog, the source type, the redshift, the S/N ratio, the normalized excess variance , the Flux in the 14-195 keV band in units A= 10^{-12} ergs s^{-1} cm^{-2} and the intrinsic and bolometric luminosity in the 14-195 keV band, in units B= ergs s^{-1}. There are 4 columns for the logarithm of black hole mass:* **1.** *$log(M_{BH,\sigma^*})$* ,**2.** *$log(M_{BH,lit})$* **3.** *$log(M_{BH}(H\beta))$* **4.** *$log(M_{BH}(H\alpha))$* **5.** *$log(M_{BH})$*